Highlights

- Geology is a major factor for Zn deficiency in soils.
- Geological factors might be related to Zn deficiency in humans.
- Residual Zn in laterite can be bound in oxides and not much of it is bioavailable.
- (A)biotic reactions with pedogenic oxides lead to strong Zn isotope fractionation.
- Zn isotopes could serve as a new tool to identify Zn deficiency in soils.

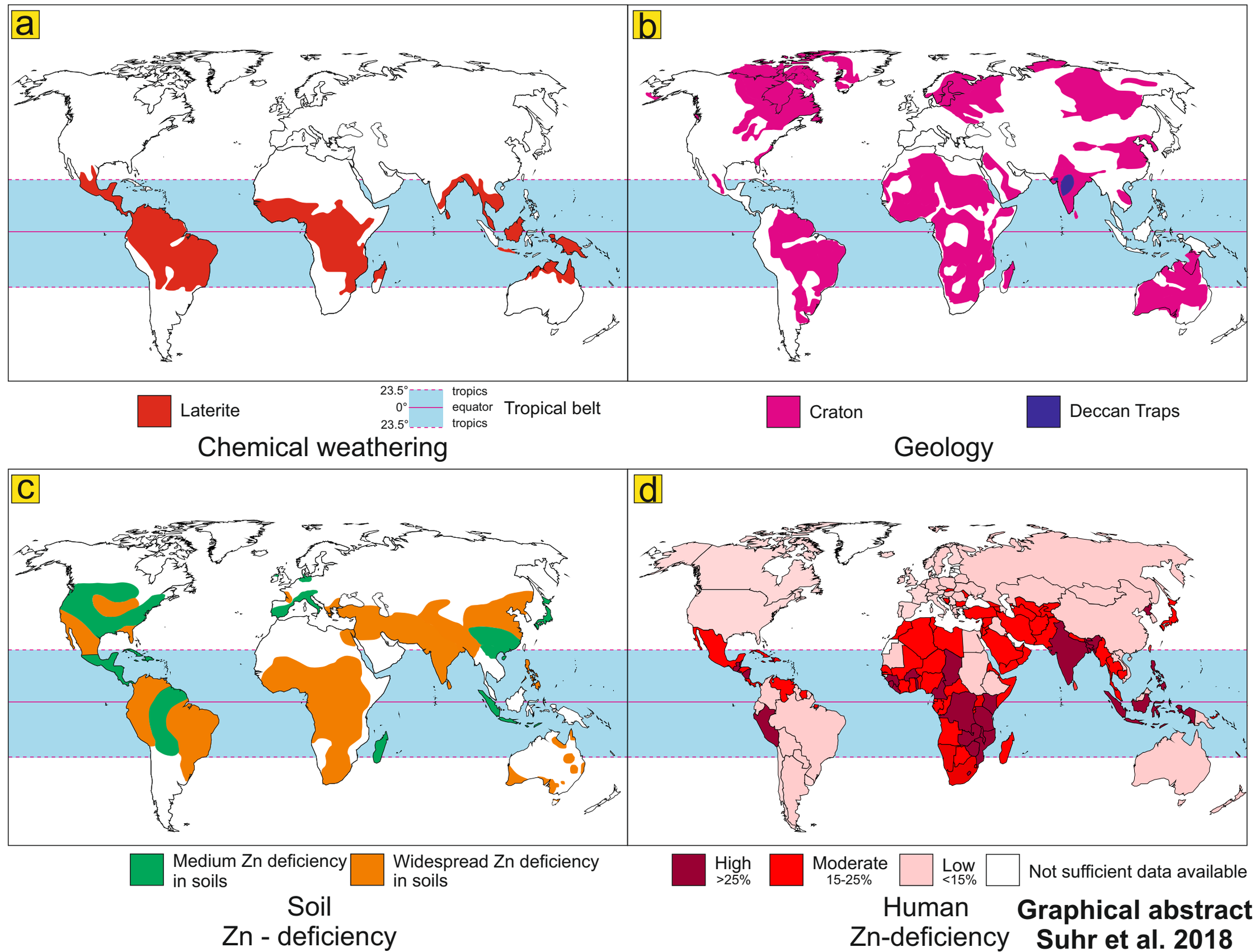
a
b
c
d
Laterite
23.5° tropics
0° equator
23.5° tropics
Tropical belt
Chemical weathering
Craton
Deccan Traps
Geology
Medium Zn deficiency in soils
Widespread Zn deficiency in soils
Soil
Zn - deficiency
High >25%
Moderate 15-25%
Low <15%
Not sufficient data available
Human
Zn-deficiency
Graphical abstract
Suhr et al. 2018

Elemental and isotopic behaviour of Zn in Deccan basalt weathering profiles: Chemical weathering from bedrock to laterite and links to Zn deficiency in tropical soils

Nils Suhr[1*], Ronny Schoenberg[2], David Chew[1], Carolina Rosca[1], Mike Widdowson[3], Balz S. Kamber[1]

[1]Geology, School of Natural Sciences, Trinity College, Dublin, Ireland

[2]Department of Geosciences, University of Tübingen, Germany

[3]Department of Geography, Environment and Earth Sciences, University of Hull, UK

*corresponding author: suhrn@tcd.ie

Keywords: Zn deficiency; soil; India; hidden hunger; malnutrition

Abstract

Zinc (Zn) is a micronutrient for organisms and essential for plant growth, therefore knowledge of its elemental cycling in the surface environment is important regarding wider aspects of human nutrition and health. To explore the nature of Zn cycling, we compared its weathering behaviour in a sub-recent regolith versus an ancient laterite profile of the Deccan Traps, India. We demonstrate that progressive breakdown of primary minerals and the associated formation of phyllosilicates and iron oxides, leads to a depletion in Zn, ultimately resulting in a loss of 80% in lateritic residues. This residue is mainly composed of resistant iron oxides ultimately delivering insufficient amounts of bio-available Zn. Moreover, (sub)-tropical weathering in regions experiencing extended tectonic quiescence (e.g., cratons) further enhance the development of old and deep soil profiles that become deficient in Zn. This situation is clearly revealed by the spatial correlation of the global distribution of laterites, cratons (Africa, India and South America) and known regions of Zn deficient soils that result in health problems for humans whose diet is derived from such land.

We also investigate whether this elemental depletion of Zn is accompanied by isotope fractionation. In the saprolitic horizons of both weathering profiles, compositions of $\delta^{66}Zn_{JMC\text{-}Lyon}$ lie within the "crustal average" of +0.27 ± 0.07‰ $\delta^{66}Zn_{JMC\text{-}Lyon}$. By contrast,

soil horizons enriched in secondary oxides show lighter isotope compositions. The isotopic depletion of Zn ($\Delta^{66}Zn_{sample\text{-}protolith}$ up to ~ -0.65‰) during the formation of the ferruginous-lateritic weathering profile likely resulted from a combination of biotically- and kinetically-controlled sorption reactions on Fe-oxyhydroxides. Our findings suggest that oxide rich soil types/horizons in sub-(tropical) regions likely exert a control on riverine Zn isotope compositions. This isotopic behaviour invites a broader study of global soils to test whether light isotope composition alone could serve as an indicator for reduced bioavailability of Zn.

1. Introduction

Zinc is an essential metal for humans, animals and higher plants because it is a structural constituent and regulatory co-factor in enzymes and proteins involved in many biochemical pathways. It is required in a wide range of macromolecules including hundreds of enzymes, and is the only metal involved in all six classes of enzymes (e.g., Alloway, 2009). In humans, Zn plays a key role in physical growth and development, the functioning of the immune system, reproductive health, sensory function and neurobehavioural development. Children suffering from Zn deficiency often show stunted linear growth, pneumonia or diarrhoea (e.g., Hotz and Brown, 2004) and it is estimated that as many as ca. 100,000 children die each year due to Zn malnutrition (Black et al., 2013). Widespread zinc deficiency is a problem in many developing countries and around 2 billion individuals of the world's human population has diets which lack in Zn (Prasad, 2012).

Zinc deficiency is considered to be the most pervasive micronutrient problem in world crops (e.g., Alloway, 2009), and the relationship to Zn deficiency in soils has been known for decades (e.g., Viets et al., 1954). In tropical and sub-tropical regions chemical weathering of rocks is the main driver for soil formation, and responsible for the release of most elements, including micronutrients such as Zn; thus, weathering profiles in (sub)-tropical latitudes make promising targets in which to explore and document processes that cause substantial element loss during soil formation. Basalts are highly reactive during weathering (e.g., Berner and Berner, 1996) and contain high concentrations of redox-sensitive metals, many of which are bio-essential. Of all common igneous rocks, basalt has the highest Zn concentration (Krauskopf and Bird, 1967; Wedepohl and Correns, 1969; Alloway, 2008), typically hosted in ferromagnesian minerals including augite, hornblende, and biotite, where it substitutes for Fe^{2+} or Mg^{2+} (Alloway, 2008).

The exchange and release of elements and isotopes in terrestrial ecosystems is determined by the complex interplay between rock, soil, biota, water, and atmosphere within the "*Critical Zone*" (CZ), which extends from the actively cycling groundwater zone up to the vegetation canopy (e.g., Brantley et al., 2007). Insight into the chemical behaviour of Zn within the CZ is essential because this zone comprises the reservoirs of soils that provide plants with nutrients. Despite the obvious role of Zn in the environment, surprisingly little is known about its elemental and isotopic behaviour during weathering. It is well documented that (bio)-geochemical cycling of metals in natural systems is often accompanied by stable isotope fractionation, and that processes including redox transformations, complexation, sorption, precipitation, dissolution, evaporation, diffusion, and biological cycling are similarly important in metal stable isotope fractionation (Wiederhold, 2015). Accordingly, stable isotope ratios have been effectively employed as geochemical tracers of pedogenic processes and associated element cycling.

Although the apparent riverine flux of Zn from unpolluted sites overlaps with the "crustal average" Zn isotope composition (Little et al., 2014, 2016; Vance et al., 2016), several studies have documented deviations in Zn isotope ratios within weathering residues. Viers et al. (2007) investigated weathering horizons of soil profiles developed on granodiorite and granite, and identified isotope fractionation leading to saprolite being ca. +0.2 permil heavier and ferruginous soil horizons being ca. -0.6 permil lighter compared to the parent granodiorite. Opfergelt et al. (2017) conducted a study of Icelandic soils derived from basalt and proposed that soil organic matter (SOM) controlled modest (0.1 permil) Zn isotope fractionation. Guinoiseau et al. (2017) studied laterite and podzol soils from the Amazon Basin and found lighter Zn in lateritic soils ($\delta^{66}Zn_{JMC\text{-}Lyon}$ = -0.11‰ and -0.14‰). By contrast, soils developed on Hawaiian basalt and Scottish granodiorite apparently show no evidence for enhanced Zn isotope fractionation (Vance et al., 2016). To date, it has remained unclear whether soil Zn isotope ratios could serve as an indicator for the extent of Zn loss and for limited bioavailability.

Here, the weathering behaviour of Zn and its isotopes on Deccan Traps basalt, India is detailed. Two weathering profiles were selected to compare their contrasting mineralogical stages of soil formation. The first is a saprolite near Chhindwara that has progressed only to a low-intermediate stage of weathering. The other is a laterite profile near Bidar, representing extreme weathering, with its uppermost levels now being almost devoid of silicates and instead replaced by a secondary mixture of chemically resistant oxides and hydroxides. The

similarity of the bedrock in both weathering profiles allows a direct comparison of the isotopic behaviour of Zn from the incipient to extreme stages of basalt alteration. Both weathering profiles have already been investigated in terms of elemental enrichment and depletion patterns, as well as with isotopic tracers (Li, Re, Os, Nd) (Kısakürek et al., 2004; Wimpenny et al., 2007; Babechuk et al., 2014; Babechuk et al., 2015), these examples provide a well-characterised opportunity to investigate elemental behaviour of Zn and Zn isotopes. The latter point is important, because previous Zn isotope studies (e.g., Viers, et al., 2007; Vance et al., 2016; Opfergelt et al., 2017) have hinted at the complex interplay of rock, soil, biota, water and atmosphere within the CZ in various climates, regions and environments on exchange reactions of Zn and Zn isotopes.

2. Geological overview, background and weathering profile descriptions

2.1 Geological overview and background

The Deccan Traps are a continental flood basalt province (CFBP) situated in northwest peninsular India; the thick lava stack was erupted onto the complex Archean–Proterozoic basement of the Dharwar craton over a period of ca. 3 to 4 Ma across the Cretaceous-Paleogene (K-Pg) boundary (Fig. 1; e.g., Courtillot et al., 1988; Widdowson et al., 2000; Chenet et al., 2007; Hooper et al., 2010; Cucciniello et al., 2015; Schoene et al., 2015). The characteristic chemical variability and isotopic signatures of this basaltic succession are well-documented and provide the basis for a detailed chemostratigraphy of 12 formations (Fm) (Mitchell and Widdowson, 1991; Widdowson et al., 2000; Vanderkluysen et al., 2011, and references therein). The Ambenali Fm, is one of the uppermost stratigraphical units, and the most geographically extensive and volumetric; importantly it is also the most compositionally homogeneous (Widdowson et al., 2000), and thus makes a very suitable candidate for case studies comparing chemical alteration and weathering processes on basalt (Kısakürek et al., 2004). Both the weathering profiles used in this study were developed on Ambenali Fm lava flow units.

2.1.1 Aggressive, tropical weathering and lateritisation of Deccan Traps basalt

The northward drift of India during the Late Cretaceous to early Cenozoic passed through equatorial latitudes (Klootwijk and Peirce, 1979; Ganerød et al., 2011) and exposed peninsular India and the Deccan Traps to aggressive tropical weathering. Extensive rainfall led to the establishment of stable water tables within the near-surface units of the neo-formed Deccan Traps flood terrain (Widdowson and Cox, 1996). This phase of alteration and

widespread lateritisation likely continued throughout the Palaeogene (Bonnet et al., 2014), diminishing by the mid- Oligocene (~25 Ma) possibly as a consequence of regional uplift coinciding with collision of India with Eurasia (Molnar and Stock, 2009) or associated regional tectonic rearrangement (Schmidt et al., 1983; Richards et al., 2016) and/or the erosive uplift of the rifted margin of Western India (Beck et al., 1995; Widdowson, 1997). As a result, these earlier developed weathering profiles were subsequently raised above the water table and dissected during the Neogene (Widdowson, 1997).

At Bidar (Fig. 1), the units of the Ambenali Formation were lateritised relatively soon after eruption (Kısakürek et al., 2004; Wimpenny et al., 2007). Several studies have found that this Bidar profile contains dust derived from extraneous sources (Kısakürek et al., 2004; Wimpenny et al., 2007; Babechuk et al., 2014; Babechuk et al., 2015) , and inputs from allochthonous groundwater only occurred during the main developmental phase of the Bidar profile: Further, any groundwater input is likely to have been locally sourced only from essentially the same, widespread basaltic units. In effect, the elevated position of the Bidar area and its remote, intracontinental location, isolates the profile from the influence of basement lithologies or marine influence (Kısakürek et al., 2004). Therefore, since influence of any compositionally different or extraneous sources has been established as negligible, the Bidar laterite profile makes an excellent candidate to investigate element mobility and its associated isotopic behaviour during advanced in situ weathering.

2.1.2 Active, (sub)-tropical weathering and geologically recent saprolitisation of Deccan Traps basalt

Large areas of the current exposure of the Deccan have not progressed to laterite, and these more recently weathered Deccan basalts are instead the result of a change to wetter climate (i.e., 'modern' monsoonal) conditions in peninsular India during the late Neogene and Quaternary (Wang et al., 2005; Spicer et al., 2017). During these Periods rivers responded by deepening and enlarging their channels, promoting increased denudation and the development of river terraces (e.g., Clift et al., 2002; Kale, 2002; Babechuk et al., 2014). The mesa-like topography of these profiles is the result of the Pleistocene–Holocene fluvial processes that incised into the flat lying, ca. 4–10 m thick basaltic flows. These fluvial processes further eroded the lateritised Palaeocene duricrust from most of the topographic highs, thus permitting variable weathering of the basalt that became exposed in the wake of climate change associated with Quaternary glacial-interglacial cycles. Currently,

approximately >90% of the current Deccan basalt outcrops consist of variably weathered basalt within saprolite-type weathering profiles 1–10 m thick.

Such a Quarternary saprolite weathering profile is exposed near Chhindwara (Fig. 1), allowing study of the incipient to intermediate stages of active basalt weathering; locally, there are no higher elevations that might unduly complicate elemental and isotopic signals resulting from the in-situ alteration processes (Babechuk et al., 2014), and only very minor input of aeolian dust has contaminated the lava flow surface during basalt emplacement. These latter have effected minimal modification of geochemical signature (Babechuk et al., 2015).

2.2 Weathering profile descriptions

Previous investigation of the Chhindwara and Bidar profiles has yielded valuable information regarding the stages of basalt chemical weathering (Babechuk et al., 2014, 2015). To provide necessary context for the current study, these may be summarised as follows:

2.2.1 Chhindwara, Deccan Traps, India (Quaternary: sub-recent profile)

This weathering profile (Figs. 1; 2a) is developed across two basalt flows exposed in a quarry east of Chhindwara, India (22° 04.213′ N, 79° 01.393′ E); its morphology and chemical composition are described in detail by Babechuk et al. (2014; 2015). Field observations show that the weathering intensity does not decrease uniformly with depth, but was partially controlled by the structure and porosity (i.e. fracturing and primary vesicularity) of the original lava flows. Accordingly, weathering is more intense at the finer-grained and banded base of the upper flow (ChQB), while the thicker, more massive central part of the upper flow is spheroidally weathered and still retains core-stones within the altered clay rich matrix; top soil is thin with limited vegetation cover. The lower flow (ChQA) has a thick (c. 10 m) massive core (now exposed by recent quarrying) which becomes progressively vesicular upwards; in the topmost 1 – 2 m these vesicles contain zeolitic amygdules.

Regardless of these physical variations, the upper parts of both the lower and upper flows exhibit essentially similar immobile element (Nb, Ta, Zr, Hf) patterns and allow an interpretation of chemical weathering trends (Babechuk et al., 2014; 2015). The least weathered samples (ChQB12, CHQB9c) are taken here as being representative of the protolith composition: ChQB9c was sampled from a corestone along with three more samples taken at increasing distance (and degree of alteration) from the corestone centre (ChQ9a, b,

d). Enhanced formation of secondary phases (smectite, hydroxides of iron, manganese oxide) is evident in the lower part of the upper flow (sample CHQB6 and downwards); examination of the overlying top soil reveals similar secondary alteration products. Similarly, these secondary phases increase towards the bottom of the lower flow with concomitant loss of primary mineralogy (clinopyroxene and plagioclase). These documented mineralogical reactions correspond with the trends of weathering indices (Babechuk et al., 2014), and demonstrate that the profile has progressed to an intermediate weathering intensity: chemical index of alteration (CIA) values of 35-80 and oxidative mafic index of alteration [$MIA_{(O)}$] values of 38-71 (Table 1).

2.2.2 Bidar laterite profile

The Bidar laterite is a deep (~50 m) weathering profile and located at a mesa edge near Bidar, India (17°54.87′ N, 77°32.39′ E) (Figs. 1, 2b). By contrast to the Chhindwara profile it exhibits a far more advanced weathering stage (Borger and Widdowson, 2001; Kısakürek et al., 2004; Babechuk et al., 2014), and is characterised by upwardly increasing degrees of alteration exposing a typical 'lateritic' weathering progression from bedrock to surface: This may be summarised as unweathered basalt (>40 m depth) passing into a saprolitic horizon (~35-30 m), advancing into saprolite with Fe-rich mottles and segregations (30-25 m); above this level primary silicates have been almost entirely transformed into secondary minerals (~25-15 m), and irregular Fe-rich agglomerations become dominant (with concomitant decrease in Si and Al concentrations); between 15-10 m depth, a zone with anomalously high Fe and trace metal concentrations is interpreted as marking the position of a former water table (Kısakürek et al., 2004; Babechuk et al., 2014; 2015); at the top the profile progresses upward from tabular, semi-indurated laterite (10-4 m) and finally into an indurated laterite cap that represents the most extreme stage of weathering. In effect, secondary clays have transformed into kaolinite, goethite and hematite in the upper portions of the profile (Fig. 2b).

The two profiles described above may be compared in the Bidar saprolite zone (BB2-BB3) where mineralogical transformations are similar to those observed throughout as in the Chhindwara profile.

3. Methods

3.1 XRD analyses

XRD analyses were performed with a Bruker D5000 at Trinity College Dublin (TCD), Ireland. Three samples of the Chhindwara profile had previously been measured with a Phillips PW 1729 X-ray diffractometer at Central Analytical Facility (CAF) at Laurentian University, Sudbury, Ontario, Canada. The methodology, analytical description, detailed descriptions of the results, quantitative mineralogy (Figs. S1-3) and petrographic descriptions of the Chhindwara bedrock samples and the Bidar laterite profiles (Figs. S4-5) can be found in the supplementary file.

3.2 LA-ICP-MS element mapping

Whereas most other analytical techniques such as elemental analysis were performed on existing samples (e.g. from the Babechuk et al., 2014 study), new samples were collected in 2016 for LA-ICP-MS trace element maps of the Chhindwara bedrock and Bidar laterite profiles. LA-ICP-MS elemental image maps were acquired using a Photon Machines Analyte Exite 193 nm ArF Excimer laser-ablation system with a Helex 2-volume ablation cell coupled to an Agilent 7900 ICPMS at the Department of Geology, TCD. The ICP-MS was tuned on NIST 612 glass as described by Ubide et al. (2015), with ThO^+/Th^+ ratios < 0.15% and Th/U ratios close to unity. Ar carrier gas and N_2 (to boost signal sensitivity) were mixed with the He-laser aerosol from the cell in a ca. 1.5 cm^3 mixing bulb which affords a rapid washout for image mapping experiments. Ten isotopes (^{7}Li, ^{24}Mg, ^{29}Si, ^{52}Cr, ^{57}Fe, ^{60}Ni, ^{63}Cu, ^{66}Zn, ^{232}Th and ^{238}U) were measured using a total duty cycle of 135 ms. A laser fluence of 3.3 J/cm^2s, a repetition rate of 31 Hz, a 12 μm spot size and a scan speed of 20 μm/s were employed. Similar to Ubide et al. (2015), image maps were made by "rastering" the sample under the ablation site. To produce the full map, adjacent lines (or "rasters") were ablated in a successive manner. The final ablated area was rectangle-shaped to facilitate production of trace-element maps using the "Image from Integrations" module in Iolite. NIST612 glass reference material was used as the calibration standard. Data reduction and production of trace element distribution maps was undertaken with the Iolite software (Paton et al., 2011) using the "Trace Elements" data reduction scheme in "Semi-Quantitative" mode (which in IOLITE corresponds to not employing an internal standard isotope). Following data reduction, trace element distribution maps were built with the Iolite module "Images From Integrations".

3.3 Elemental analysis

Samples from the Chhindwara profile (n=27; Babechuk et al., 2014) were powdered in an agate mill while the powders for the Bidar profile were prepared in a tungsten carbide mill. The major element composition of both profiles was determined by X-ray fluorescence (XRF) following a loss-on-ignition (LOI) measurement; the Bidar XRF data were obtained at the Open University (UK) and were reported previously (Kısakürek et al., 2004; Widdowson, 2007). The Chhindwara XRF data were obtained at Geoscience Laboratories (Sudbury, Ontario). Ferrous iron measurements were also obtained on Chhindwara samples at the Geoscience Laboratories via potentiometric titration with potassium permanganate and were reported in Babechuk et al. (2014). All trace element data were obtained via solution quadrupole ICP-MS analysis at the Department of Earth Sciences at Laurentian University (LU) with a Thermo Scientific XSeriesII (LU) and at TCD with a Thermo Scientific iCap-Qs. Tantalum, W, and Mo data were not reported for the Bidar samples due to potential contamination from the tungsten carbide mill, but all other trace elements are unaffected (Babechuk et al., 2015). For further information on sample preparation and analysis, readers are referred to the original studies (Kısakürek et al., 2004; Babechuk et al., 2014; 2015). Total organic carbon (TOC %) analyses were undertaken using an Elementar vario EL cube instrument at the Trinity Centre for the Environment, TCD.

3.4 Analytical technique for zinc isotope determination

Zinc isotope analyses were performed at the Isotope Geochemistry Group, Eberhard Karls University Tuebingen, Germany. The protocol for Zn purification is detailed in (Moeller et al., 2012). Powder aliquots of soil samples and USGS rock reference materials containing at least 1µg of Zn were spiked with an appropriate amount of purified ^{64}Zn-^{67}Zn double-isotope tracer prior to digestion with HF-HNO_3 (Moeller et al., 2012). The double-spike technique allows the in-run correction of instrumental mass-bias effects but also accounts for Zn isotopic fractionation caused by anion-exchange chemistry (Bermin et al., 2006). The digests were converted to chloride for ion chromatography using self-made Teflon shrink columns loaded with 1.1 mL of BioRad DOWEX AG MP-1, 100-200 mesh anion resin. Procedural blanks were below 1 ng total Zn and therefore were negligible.

Zinc isotope ratio measurements were performed on a ThermoFischer Scientific Neptune Plus MC-ICP-MS, in low resolution mode, coupled to a Cetac ARIDUS II. The Aridus II desolvating nebulizer system greatly reduces potential metal-oxide interferences on Zn

masses in the analyte solutions, such as $^{52}Cr^{16}O$ on ^{68}Zn, $^{51}V^{16}O$ on ^{67}Zn, $^{50}Cr^{16}O/^{50}V^{16}O/^{50}Ti^{16}O$ on ^{66}Zn and $^{48}Ti^{16}O$ on ^{64}Zn, although impurities of Ti, V, and Cr have never been detected. To avoid any metal-nitride formation the Aridus II was run without additional N_2 gas. Signals of $^{64}Zn^+$, $^{66}Zn^+$, $^{67}Zn^+$, $^{68}Zn^+$ and $^{70}Zn^+$ together with the interference monitors $^{62}Ni+$ (for correction of $^{64}Ni+$ on $^{64}Zn+$) and $^{72}Ge+$ (for correction of $^{70}Ge+$ on $^{70}Zn+$) were detected simultaneously. Small background signals (e.g. very small signals from long-term memory of the uptake system, the Ni cones or the sample carrier solution) were corrected with on-peak zero measurements of the sample carrier solution prior to each measurement. A 10^{10} Ω resistor was used to detect the highly abundant ^{64}Zn signal (49.2% natural abundance plus enriched ^{64}Zn from the double spike), a 10^{12} Ω resistor was used to detect the least abundant ^{70}Zn (0.61% natural abundance) and all other signals were detected using 10^{11} Ω resistors on the respective amplifiers. The double spike deconvolution was performed using measured abundances of the ^{64}Zn, ^{66}Zn, ^{67}Zn and ^{68}Zn isotopes. The lowest signal intensities are detected on $^{68}Zn^+$ when using a ^{64}Zn-^{67}Zn double spike and 1:1 sample to DS ratios. During the course of this study signals detected on $^{68}Zn^+$ ranged between 1.5 and 6.4 V using an amplifier resistor of 10^{11} Ω allowing for high-precision Zn isotope ratio analyses.

Isotopic data are reported in the δ notation relative to the certified $\delta^{66/64}Zn_{IRMM\text{-}3702}$ solution standard. For ease of reference, they are also tabulated (Table 1) relative to the "JMC-Lyon" solution standard using an offset of +0.29 ± 0.05‰ (Moeller et al., 2012). The external 2 s.d. reproducibility for $\delta^{66}Zn$ on IRMM-3702 during the course of his study was better than 0.03‰. Accuracy was controlled by interspersed analyses of an in-house solution standard prepared from an "Alfa Aeser" Pura-tronic Zn wire yielding an average $\delta^{66}Zn$ of -10.295 ± 0.026‰ (2SD, *n=8*), within the laboratory long-term reproducibility of -10.278 ± 0.051‰ (n=21). The USGS standards BCR-2, BHVO-2, and BIR-1a yielded average $\delta^{66/64}Zn_{JMC\text{-}Lyon}$ values of 0.280 ± 0.036‰ (*n=3*), 0.315 ± 0.036‰ (*n=3*) (supplementary table), and 0.236 ± 0.028‰ (*n=6*), respectively. These are within the range reported in previous studies (Sossi et al., 2015), demonstrating the accuracy of this dataset.

4. Results

4.1 XRD data

The quantitative XRD mineralogy of the Chhindwara profile (Fig. 3a) shows that minor amounts of smectite developed at the base (ChQB6) of the upper flow (Fig. 3a). Further

down the weathering profile, in the lower volcanic flow, the amount of smectite increases, whereas the amounts of primary clinopyroxene and plagioclase decrease. The amount of smectite decreases somewhat only in the deepest levels of the lower volcanic flow probably as a result of the textural control on the extent of weathering (Babechuk et al., 2014). In general identification and quantification of those phases which have undergone moderate weathering can be challenging; here materials consists of amorphous clays, secondary oxides and volcanic glass that cause strong background signals (see supplementary for more information in the diffractograms). Results should, therefore, be interpreted only as a qualitative estimate of the mineralogical composition.

In the Bidar profile, plagioclase, clinopyroxene and magnetite are the primary mineral phases (Fig. 3b). In sample BB3, enhanced formation of kaolinite is evident, whilst in sample BB4, primary silicates have been transformed entirely to secondary clays (mainly kaolinite) and Fe-oxides (hematite, goethite, Fe-oxyhydroxides). From section BB4 to BB5, slightly higher quantities of Fe-oxides were measured, whereas at the palaeowater-table sample (BB6) > 90% of Fe-oxides, particularly goethite, are recorded. Above this level, the weathering progresses as expected, with kaolinite decreasing as Fe-oxides increase upwards to the tubular/nodular cap (BB9). This nodular cap contains more than 90% Fe-oxides.

4.2 LA-ICP-MS element maps

Thin section petrography shows that the parent dolerite rock of the lower flow is mainly composed of clinopyroxene, plagioclase, volcanic glass, and Fe-Ti oxide (Figs. S4, S6). The LA-ICP-MS element maps show that Zn was mainly hosted within the primary Fe-Ti oxide, pyroxene and volcanic glass (Fig. S6b). The concentration of Zn and Mg are lower in the weathered Mg-Fe silicate (Fig. S7) than in unaltered clinopyroxene (Fig. S6), whereas the concentration of Fe is higher. In the bedrock of the Bidar laterite, Zn is mainly hosted within pyroxene and primary Fe-Ti oxide (Fig. S8a). In the palaeo-watertable sample, Zn is enriched in the Fe-oxyhydroxides (Fig. S8b). In the nodular cap on top of the profile (Fig. S8c), Zn is mainly depleted in Fe-oxyhydroxide rich areas, with the exception of a small vein that exhibits similar Zn enrichment as the Fe-oxyhydroxides in the palaeo-watertable sample.

4.3 Transition metals (Zn, Fe^{III}/Fe^{II}, Mn) and MgO (wt. %) in the Chhindwara saprolite profile

Various transition metal ratios and MgO abundances are presented in Table 1 and Fig.4. Babechuk et al. (2015) showed that the high field strength element (HFSE) ratios of Zr/Hf

and Nb/Ta do not deviate by more than 3% in all samples within both flows of the Chhindwara profile. Niobium and Ta were found to be the least-mobile elements for mass calculations (see also Kurtz et al., 2000). Therefore, Zn, Fe and Mn concentrations were normalised to Nb. In contrast to Nb, Zn exhibits greater mobility within both flows of the Chhindwara profile and in most cases the Zn/Nb ratios of the weathered samples are lower compared to the Zn/Nb ratios of unweathered protolith (ChQB12; Table 1, Fig.4).

Overall, the chemostratigraphical trends of Zn/Nb and MgO (wt. %) are similar. This is particularly obvious at the weakly banded base of the upper flow (lowermost 80 cm), where diminished release of MgO (wt. %) is accompanied by minor loss of Zn (samples ChQB3 and ChQB2). Enrichment of Fe(III) and Mn also occurred in this weakly banded base (Fig.4 c, d). By contrast, in both top soil samples from this flow (ChQB10 and ChQB11), Mn/Nb is depleted, whereas Zn/Nb in ChQB10 is slightly enriched. In the less weathered formerly columnar central section of the upper flow, a modest enrichment in Zn/Nb is linked to slightly higher MIA values of 41 and 50 in samples ChQB7 and CHQB9d respectively. In the lower flow, from top to bottom of the profile, Zn/Nb as well as MgO (wt. %) are more strongly depleted than in the less weathered upper flow. However, fluctuations in the depletion trend of Zn/Nb are found which correlate with the weathering trend of Mn/Nb.

Weathering trends based on elemental mass-balance calculations are listed in Table 1, whereby the change in an element of interest is expressed relative to the least-weathered parent rock (ChQB12). The respective loss and gain of an element in a sample is calculated after normalisation to an immobile or least-mobile element for both the sample and the parent rock in the formula (Table 1; e.g., Brimhall and Dietrich, 1987; Kurtz et al., 2000; Kisakürek et al., 2004; Babechuk et al., 2015).

$$\% \text{ change in R} = \left[\frac{(Rsample - Rprotolith)}{Rprotolith}\right] x\ 100$$

The Zn/Nb ratio within the upper flow indicates a deviation from the protolith of ~ -14% to +5%. Stronger fluctuations are evident for Mn of ~ -16% to +43%. A sharp depletion trend of Zn and Mn marks the transition between the upper (ChQB) and lower flow (ChQA) and the enhanced release of Zn correlated with increased weathering intensity is evident. The loss corresponds to deviation from the protolith of between ~ -13% to -36% for Zn and -23% to -60% for Mn, respectively.

382 *4.4 Zn and Fe_2O_3 (wt. %) in the Bidar profile*

383 The Zn and Fe_2O_3 (wt. %) results are presented in Table 1 and Fig. 5, with Zn normalised to
384 Nb. Fe_2O_3 (wt. %) is not plotted *vs* an immobile element, since it itself is an immobile
385 element in the oxidative environment. From the bedrock upwards into the indurated laterite
386 cap, an overall depletion trend in Zn/Nb is evident. The exception is the iron dominated
387 palaeo-watertable sample, where Zn/Nb is enriched. Generally, with strengthening
388 weathering intensity, the amount of Fe_2O_3 (wt. %) increases, resulting in a maximal
389 enrichment of Fe_2O_3 (77.5 wt. %) in the strongest weathered section, i.e. the top of the
390 nodular cap (BB9). Excluding the palaeo-watertable sample (BB6), Zn concentrations are
391 moderately anti-correlated with Fe_2O_3 (wt. %) ($r^2 = 0.65$; not shown). When expressed
392 relative to the least-weathered parent rock, a maximum loss of ca. 80% in Zn is calculated for
393 the most weathered section of the lateritic profile (BB9), whereas the palaeo-watertable
394 (BB6) is enriched by ~ 250% (Table 1). In general, the TOC is low in the Bidar profile (Table
395 1; Fig.5d). Starting from the bedrock sample (BB1) with a TOC of 0.07%, TOC increases
396 moderately upwards with the exception of samples BB4 (0.51%) and BB9 (0.32%) that are
397 relatively enriched compared to the protolith.
398

399 *4.5 Zn isotopic composition in both profiles*
400 The Zn isotope data are presented in Table 1 and Figures 4 and 5. Differences in the
401 $\delta^{66}Zn_{JMC\text{-}Lyon}$ composition relative to the protolith ($\delta^{66}Zn_{sample} - \delta^{66}Zn_{protolith}$) are expressed as
402 $\Delta^{66}Zn_{sample\text{-}protolith}$ and tabulated (Table 1). In the Chhindwara saprolite profile (Fig.4e), the
403 parent basalt has a $\delta^{66}Zn$ value of +0.260 ± 0.018‰ (2 SE) relative to JMC Lyon standard.
404 The values of $\delta^{66}Zn_{JMC\text{-}Lyon}$ in the Chhindwara saprolite profile range from +0.190 ± 0.024‰
405 to +0.289 ± 0.020‰. The degree of isotope fractionation across the entire profile is very low
406 outside of external reproducibility.

407 In the Bidar laterite profile (Fig.5c), the parent basalt has a $\delta^{66}Zn_{JMC\text{-}Lyon}$ value of +0.231 ±
408 0.014‰ (2 SE), very similar to the Chhindwara bedrock. The saprolitic, clay-rich zones
409 (BB2-BB3) also exhibit a very low degree of isotope fractionation, respectively, whereas in
410 the more strongly weathered, secondary Fe-oxide rich part, lighter Zn compositions are
411 found. In particular, the palaeo-watertable (BB6) and nodular cap (BB9) samples that are
412 very strongly enriched in Fe-oxides are depleted, with $\Delta^{66}Zn_{sample\text{-}protolith}$ values of -0.660‰
413 and -0.514‰, respectively. Furthermore, sample BB4 exhibits a lighter Zn isotopic

composition with a $\Delta^{66}Zn_{sample\text{-}protolith}$ value of -0.478‰, while samples BB5 (-0.091‰), BB7 (-0.013‰) and BB8 (-0.115‰) show less fractionated Zn isotope compositions compared to the protolith value. In summary, the Bidar profile becomes enriched in lighter Zn isotopes towards the top, even though excursions within this overall depletion trend are evident. All Zn isotope data are interpreted using the laboratory long-term reproducibility of the in-house solution standard (2SD = ±0.051‰) to apply the highest analytical uncertainty.

5. Discussion

In the following sections, elemental and isotopic trends of Zn in both profiles are interpreted in conjunction with the quantitative XRD mineralogy (Fig. 3), the LA-ICP-MS element maps (Figs. S6-8), weathering indices (CIA, $MIA_{(O)}$) as well as selected major element abundances (Fe, Mn; Table 1). As the Bidar profile involves an older, more complex and more prolonged weathering history, additional chemostratigraphic information (TOC values and previously published elemental dust signatures (Nd, Th, U) (Fig., 5e) from Babechuk et al. (2015) are also compared to the Zn isotope systematics, to help elucidate the different environmental processes that were involved in laterite formation and to understand which mineral reactions promoted Zn mobility. In the final section, we discuss the relevance of the observed Zn behaviour within the hydrosphere and anthroposphere.

5.1 Chhindwara saprolite profile- Zn and Zn isotopes

The LA-ICP-MS maps of the Chhindwara bedrock provide evidence that primary Fe-Ti oxides host the highest concentrations of Zn. They are unlikely to contribute to Zn loss because of their strong resistance to weathering (e.g., Nesbitt and Wilson, 1992). By contrast, clinopyroxene is a major carrier and volcanic glass a minor carrier of Mg, where Zn^{2+} substituted at trace concentrations for Mg^{2+}. The breakdown of pyroxene and volcanic glass resulted in release of both elements beginning with incipient weathering (Figs. S6, S7). This explains the coupled behaviour of Zn/Nb ratios with MgO% in the upper flow of the profile. In the lower flow, greater amounts of Zn and MgO% have been released, but Zn/Nb correlates with Mn/Nb ratios, which points to a minor association of Zn with a Mn-rich phase (Fig. 4). Additionally, the minor release of Zn in areas of Mn/Nb and Fe^{III} enrichment at the weakly banded base of the upper flow, suggests coupled behaviour between Zn and secondary oxides.

Regardless, the release of Zn is mainly associated with the chemical breakdown of the Mg-rich phases (pyroxene: ~ 120 µg/g and volcanic glass: < 40 µg/g) that became converted into smectite and secondary oxides (Figs. 3a, 4, S6, S7). Overall, this means that a net loss of Zn occurred as a result of these mineral transformations. This is also confirmed by the CIA values that lie within the range of smectite in the more strongly weathered sections (values between 70-85) (Nesbitt and Young, 1982; Nesbitt and Wilson, 1992) and its correlation with the MIA(o) (Table 1; Fig.4), indicating the similar bulk weathering behavior of Mg, Ca, and Na in the profile ($R^2 = 0.9$; Babechuk et al., 2014). As a result of this alteration, ca. 35 % of the mobile Zn fraction was lost from the more strongly weathered part of the saprolite.

In the top soil, biological processes might explain the very slight enrichment of Zn (CHQB10) via adsorption or complexation with soil organic matter (SOM), while Zn depletion (ChQB11) was possibly caused by preferential uptake into vegetation. Atmospheric inputs into the top soil are unlikely because the addition of dust to the profile was minimal (Babechuk et al., 2015).

Zn isotopic fractionation remains within the analytical uncertainty (2SD) of the protolith and overlaps with the "crustal average" of $\delta^{66}Zn_{JMC\text{-}Lyon}$ (+0.27 ± 0.07‰) (Little et al., 2016). This implies that the flux of elemental Zn to the hydrosphere from saprolite and incipient weathering fronts of Deccan basalt (deeper CZ) has an isotopic composition within the range of "lithospheric" Zn (e.g., Little et al., 2014).

5.2 Bidar laterite profile - Zn and Zn isotopes

The lower sections of the profile (BB2-BB3) display similar elemental and isotopic weathering behaviour of Zn comparable to the Chhindwara profile and only a slightly higher loss of Zn (ca. 45%) in BB3 is evident. By contrast, the more extreme weathering intensity in the upper sections of the Bidar profile resulted in a Zn loss of up to 80% (BB5, BB9) and lighter Zn isotope compositions developed. Based on the quantitative mineralogical analyses (Fig. 3b), the loss of the additional 35% of Zn in the upper sections of the Bidar profile must be related to the transformation from smectite to kaolinite and Fe-oxides (hematite, goethite, and iron-oxyhydroxides). The critical role of the mineralogical transformations from bedrock to laterite can be further visualised by detailed petrography and the LA-ICP-MS trace element maps, which illustrate that the secondary Fe-oxides exhibit an inherently low Zn content in the lateritic weathering residue (Figs., S8a, c). This is also confirmed by the enrichment in Fe_2O_3 (wt. %) and decreasing Zn/Nb ratios towards the top of the profile (Fig.

5). An exception to the overall depletion trend of Zn is represented by the palaeo-watertable (Figs. 3, 5, S8b), where anomalous Zn enrichment of 252 % is evident (sample BB6, Table 1). This is explained by the iron oxide enrichment in this sample that likely resulted from a significant net input of groundwater-transported Fe^{2+} and oxic rainwater, which facilitated the oxidation to Fe^{3+} and subsequent precipitation as ferric oxides (e.g. Kısakürek et al., 2004). Thus, the same process may have resulted in the enrichment of Zn.

The relationship between Fe oxide development and Zn mobility is also reflected by the Zn isotopic fractionation in horizons that are enriched in Fe_2O_3 (wt. %) (Table 1). Fractionation resulted in depleted values up to 13 times larger than analytical uncertainty (2SD). Excluding sample BB4, increasing lighter Zn isotope ratios correlate strongly with Fe_2O_3 (wt. %) (R^2 = 0.944; Fig. 6a), whereas a moderate correlation is evident for all samples (R^2 = 0.622). The oxyhydroxide development may be associated with the retention of lighter Zn ($\Delta^{66}Zn_{sample\text{-}protolith}$ of up to -0.660‰ in the palaeo-watertable).

However, the deviation of sample BB4 from the correlation trend (Fig. 6a) suggests that a first order relationship between oxyhydroxide development and the extent of fractionation towards lighter $\delta^{66}Zn_{JMC\text{-}Lyon}$ is not necessarily always linked. In the following section, the possible pedological processes in laterite are discussed and contrasted with the sub-recent, clay rich Chhindwara saprolite profile.

5.3. Processes affecting the Zn isotope composition in laterite

5.3.1. The impact of abiotic weathering processes on isotopic Zn

In general, the preferential adsorption of lighter Zn on secondary oxides in weathering profiles (Viers et al., 2007; Vance et al., 2016; this study) contradicts most experimental studies. In such studies, heavier Zn isotopes adsorb on iron-oxy-hydroxide (Juillot et al., 2008; Pokrovsky et al., 2005). Only in the early stages of such experiments is adsorption of isotopically lighter Zn on the surfaces sites observed and explained by short-lived kinetic isotope effects. After a relatively short time, however, the experiments evolve to steady state (*i.e.* equilibrium fractionation) and to high ionic strength, with preference to heavier Zn on the mineral surfaces. Since the ionic strength in laterites is low (e.g., Robson and Gilkes, 1980, Dolling and Ritchie, 1985, Chairidchai and Ritchie, 1990), the preferential adsorption of lighter Zn on the surface sites of secondary oxides is possible. Such a pedological process might also cause the incorporation of lighter Zn into secondary oxides. However, the strong fractionation towards lighter Zn in the metal enriched palaeowater-table sample (BB6) is not

explainable with this process, so we propose that two different mechanisms might be responsible for the enrichment in lighter Zn isotopes.

Firstly, pH-dependent sorption experiments ($3 < pH < 8$) on goethite surfaces (Pokrovsky et al., 2005) showed enrichment of lighter Zn by 0.1-0.3 ‰ with decreasing pH values. Lateritic soils develop in low pH (2-5) environments (e.g., Wimpenny et al., 2007) and the oxidation of Fe^{2+} to Fe^{3+} results in a release of protons into solutions. This means that the formation of secondary Fe-oxides exerts a control on decreasing pH and may explain the isotope fingerprint in the goethite-rich palaeowater-table (Figs. 3b, S8b) or nodular cap (BB9) of the Bidar profile. However, it must be noted that the adsorption of lighter Zn on goethite might be alternatively related to short-lived kinetic effects (Moynier et al., 2017) and that it was not confirmed in other pH experiments (e.g., Julliot et al. 2008). Secondly, changes in the redox state of the Bidar profile might have caused the lighter Zn composition in the palaeowater-table sample (BB6). For instance, spinel and chromite have lighter Zn compositions (Luck et al., 2005; Chen et al., 2013). The dissolution of Fe^{2+} from such refractory phases in reducing environments below the water table could have vertically transported lighter Zn upwards the profile where it precipitated with Fe oxides.

Regardless of the mechanisms responsible for the formation of Fe-oxyhydroxides in laterite, the absence of such processes in younger, clay rich weathering substrates from the deeper CZ (Chhindwara profile and Bidar saprolite) might explain the lack of Zn isotope composition departing significantly from the crustal average (Little et al., 2016). The enhanced formation of Fe-oxyhydroxides is therefore one key process to explain Zn isotope fractionation towards lighter values.

5.3.2 The significance of biotic processes on isotopic Zn in the Bidar laterite profile

The increasingly open and porous structure of the profile upwards from BB4 to BB9 (Babechuk et al., 2015) provides pathways for mobile colloidal particles in percolating meteoric water, and the chemostratigraphical trends of TOC and $\delta^{66}Zn_{JMC\text{-}Lyon}$ demonstrate a likely association (Fig. 5c, d). This relationship is as also evident from the inverse correlation of lighter $\delta^{66}Zn_{JMC\text{-}Lyon}$ with higher TOC ($r^2 = 0.421$; and $r^2 = 0.764$, excluding the palaeo-water table sample BB6; Fig. 6b). The reddened, kaolinite rich saprolite section of the Bidar profile (BB4) contains the highest TOC % of all samples and departs from the positive correlation trend of lighter $\delta^{66}Zn_{JMC\text{-}Lyon}$ with Fe_2O_3 (wt. %) (Fig. 6a). Hence, biochemical reactions likely affect fractionation of Zn isotopes and possibly its association with specific soil minerals. Zinc is normally complexed to organic ligands in soil solutions and Vance et

546 al. (2016) and Opfergelt et al. (2017) suggested that they can preferentially transport heavier
547 Zn out of soils. This is in agreement with experimental studies which have shown that Zn
548 adsorbs on humic acids, resulting in a Zn pool heavier than the corresponding free aqueous
549 ion by 0.25‰ (Jouvin et al., 2009). Apart from that, Houben et al. (2014) demonstrated that
550 heavier Zn isotopes are preferentially retained in roots of plants ($\Delta^{66}Zn_{root-shoot}$ = +0.24 to
551 +0.40‰). As a result, the residual soil solution contains isotopically lighter Zn that may
552 adsorb on mineral surfaces. The loss of heavier Zn through mobilisation of solid organic
553 material (Vance et al., 2016) and lighter Zn soil solutions are potential mechanisms to explain
554 the lighter Zn composition in the ferruginous sections of the Bidar profile. However, the
555 previously outlined abiotic fractionation mechanisms suggest that biotic fractionation alone is
556 unlikely to explain the lighter compositions in samples BB4 and BB9 ($\Delta^{66}Zn_{sample-protolith}$ ~ -
557 0.5‰).
558
559 *5.3.3 Dust addition and redistribution of elemental and isotopic Zn*
560 Aeolian dust input is a likely means of altering elemental and isotopic compositions in the
561 Bidar profile, especially where input material is of significantly different composition and
562 antiquity to that of the basalt protolith. Further, the documented extent of dust addition is not
563 limited to the topsoil (Babechuk et al., 2015), and dust appears to have been washed into the
564 porous and tubular layers that characterise the upper portions of the laterite profile.
565 Potentially, Zn, as well as Fe could at least partly be derived from aeolian dust sources (e.g.,
566 Taylor et al., 1983; Gallet et al., 1996; McLennan, 2001). Importantly, inspection of the trace
567 element maps of Fe and Zn from the nodular cap (BB9) reveals a strong enrichment of both
568 elements on the microscale in Fe-oxide rich veins (Fig. S8c). These could represent
569 segregation pathways of dust-derived material into the laterite (Widdowson, 2007).
570 Several sections (BB 3, 5, 6, 7, 8, 9) of the Bidar laterite show complex enrichment
571 and redistribution trends of U, Nd, and Th, which were at least in part attributed to dust input
572 (Fig.5e; Babechuk et al., 2015). Zinc concentration shows a relationship to Th in the topmost
573 samples of the laterite (BB7–BB9). In combination, the trace element maps and
574 chemostratigraphical trends therefore suggest that whilst dust-derived Zn has likely entered
575 the profile, it did so without causing the relative enrichment intensities observed for other
576 elements.
577 According to Little et al. (2014; 2016), average dust $\delta^{66}Zn_{JMC-Lyon}$ values lie between
578 +0.33 and +0.37‰. These values are similar to the Bidar bedrock within analytical
579 uncertainty, whereas aerosols from tropical latitudes can be ca. +0.2‰ heavier (Little et al.,

2014). An "isotopic overprint" from such sources might explain why the $\delta^{66}Zn_{JMC\text{-}Lyon}$ of BB7 is nearly indistinguishable from the Bidar bedrock or why sample BB3 illustrates a slight offset from the linear regression line towards heavier Zn isotope value (Fig. 6a) Regardless, the palaeo-water table sample (BB6) is characterised by the highest allochthonous input to the profile and exhibits the lightest Zn isotope composition in the profile. In summary, despite evidence for aeolian input, the previously described in situ pedological processes likely dominated the isotopic evolution of Zn in most sections of the Bidar profile.

5.4 Relevance for Zn deficiency in crops grown in (sub)-tropical environment

Mineralogical transformations in the weathering process ultimately lead to inherently low Zn contents in laterite and, depending on the type of soil classification system, also in ferralsols and oxisols elsewhere (Fig. 5a, b). With respect to the availability of Zn to plants, it is noteworthy that much of the remaining residual pool of Zn remains bound in refractory phases: either within primary oxides, or in the weathering products hematite, goethite, and iron-oxyhydroxides (Figs. 3b, 5a, b, S8) (e.g., Nesbitt and Wilson, 1992). As a result, the supply of Zn to plants can be severely limited on lateritic soils, even when a residual Zn pool is present. This is one reason why even Zn-rich bedrock, such as basalt, can develop into a residue with inherently low bioavailable Zn.

The trace element maps presented in this study illustrate this scenario. In samples where Zn is hosted by refractory minerals, measurement of the subsoil Zn concentration via assay alone is not sufficient to determine the quantity of bioavailable Zn. The relatively spare available data, including the results from this study, suggest that light Zn isotope composition in subsoil may be an indication of poor bio-availability of Zn. By contrast, subsoil Zn isotope ratios within the crustal average (e.g., Little et al., 2014; 2016) may show that the inorganic pool of bio-available Zn has not been evacuated from the soil reservoir. Thus, there is potential that Zn isotopes may eventually serve to fingerprint subsoils with poor Zn bioavailability.

A striking result of global geochemical and soil distribution atlases is that the CZ in many tropical and subtropical regions is strongly depleted in most bio-essential elements (Fyfe et al., 1983). We propose that this is not solely due to the climatic control on the type of weathering but also because stable continental regions (cratons) underlie these soils. Cratons are characterised by remarkable tectonic quiescence with resulting low denudation rates (e.g., Hewawasam et al., 2013). In (sub-)tropical regions, they are typically covered by laterite

residues. Fresh bedrock and/or smectite rich regolith of the deeper CZ is only rarely exposed at the surface of cratonic regions of India, Africa, South America, and Australia. The development of widespread and stable laterite in such areas severely limits the natural re-supply of Zn from fresher rock material at depth.

We further propose that it is not a coincidence that Zn deficient soils (Alloway, 2008), highly depleted weathering residues (i.e. laterite soils) (Gidigasu, 2012 and references therein), and cratons (USGS, 1997; Tang et al., 2013) show general geographic superposition within the tropical belt (graphical abstract). Agricultural cultivation in these areas may therefore be inherently challenging in terms of micronutrients, with knock-on effects such as growth abnormalities (e.g., Alloway, 2009); including stunted growth, small leaves and sterility, increased susceptibility to damage by high light intensity, as well as propensity for fungal infection (e.g., Cakmak, 2000; Alloway, 2009). Zn deficiency in subsistence farmers in subtropical-tropical cratonic areas may be magnified by their over-dependence on crops local for diet (graphical abstract; Wessells and Brown, 2012; Andersen, 2002).

Finally, at least in some areas (e.g. the Amazon) the isotopically light Zn of weathering residues is possibly mirrored by heavy values in the dissolved load of rivers (e.g. $\delta^{66}Zn_{JMC\text{-}Lyon}$ ca. +0.5-0.6‰; Little et al., 2014). This suggests that analysis of (sub)-tropical river waters might be an alternative and logistically feasible way to gain valuable information on soil Zn deficiency in entire catchments from geologically challenging areas.

6. Conclusions

Our new elemental Zn and Zn isotope systematics from two contrasting weathering profiles from India have resulted in the following main findings:

1) In the sub-recent, smectite-rich Chhindwara saprolite only a small fraction of bio-available Zn has been evacuated, and Zn isotopes remained almost unchanged during weathering. By contrast, Zn is strongly fractionated in the highly weathered upper sections of the Bidar laterite, likely from a number of (a)biotic processes ($\Delta^{66}Zn_{sample\text{-}protolith}$ up to ca. -0.65‰). Enhanced formation of secondary Fe-oxyhydroxides is a requirement for fractionation towards lighter Zn ratios, while the TOC in a ferruginous, kaolinite rich section of the profile suggests that biotic processes exert control on the Zn isotope systematics as well. In both scenarios, the fractionation towards lighter Zn ratios in the subsoil develops in the absence of fertile rock debris and smectite.

2) LA-ICP-MS trace element maps are a powerful tool to investigate the mineral hosts of bio-essential trace elements in the CZ. In the Bidar laterite profile, high quantities of Zn are locked away in weathering resistant primary oxides and refractory secondary oxide phases. Hence, bulk soil analyses and depletion factors alone are not reliable indicators by which to assess the amount of bio-available Zn in soils.

3) Even on originally Zn rich bedrock, subtropical-tropical cratonic soils may experience Zn deficiency, as evident from world maps. Surface layers become severely leached and, depending on the bedrock, soils will be dominated by minerals such as gibbsite, Fe-oxides, kaolinite and quartz (see Fyfe et al., 1983). Due to the tectonic quiescence of cratonic areas, they remain covered by severely leached surface layers in the subtropics and tropics. Geology and weathering history evidently contribute to human Zn deficiency in areas where the population relies on local crops.

4) Because the Zn isotope ratios in the Chhindwara saprolite and strongly weathered upper sections of the Bidar laterite differ, Zn isotopes could eventually serve as new tool to evaluate the overall loss of Zn and storage of bio-unavailable Zn in oxides. The investigation of Zn isotopes in subsoils and rivers that drain these areas might therefore help to improve sustainable farming practices in subtropical-tropical cratonic regions where vast areas are covered by challenging soils.

Acknowledgments

This work is a contribution from the Marie Curie Initial Training Network IsoNose (www.IsoNose.eu) that is funded by the People Programme (Marie Curie Actions) of the European Union's Seventh Framework Programme FP7/2007-2013/ under REA grant agreement no [608069]. Dr. Robbie Goodhue assisted in XRD measurements and Mr. Mark Kavanagh in TOC measurements. We thank Dr. Michael G. Babechuk for Zn concentration measurements and the editorial input of Prof. Mae Sexauer Gustin. The final manuscript significantly benefitted from the suggestions of three anonymous reviewers.

Figure captions

Fig.1 Simplified geological map showing the extent of the Deccan Volcanic Province (DVP) within peninsular India and the geomorphology of the weathered basaltic terrane. Inset maps

show (a) the mesa topography near Chhindwara in the Madya Pradesh district and (b) the more detailed geology of the SE lobe of the DVP, including the extent of the thick laterite that hosts the Bidar profile (Babechuk et al., 2014). DVP geology maps are modified from Borger and Widdowson (2001), Kısakürek et al. (2004) and Babechuk et al. (2014).

Fig.2 Geological sketch section of the: a) Chhindwara weathering profile b) Bidar laterite (modified from Kısakürek et al., 2004 and Widdowson, 2007). The mineralogy in the weathering progression accompany the schematic of each profile and is discussed in the next chapters.

Fig.3 Quantitative XRD bulk mineralogical determination of the Chhindwara saprolite profile (a) and Bidar laterite profile (b). The stacked horizontal bar charts represent the identified mineral phases and their respective quantities in each weathering section. Note that the quantities in Chhindwara are unlikely to reflect the correct quantities of the identified minerals, due to strong background signals as a result of amorphous phases (some clays and secondary oxides). Regardless, high quantites of smectite have been identified and agree to the findings of previous studies (Babechuk et al., 2014; 2015). For further information see also the supplementary information.

Fig.4 Chhindwara saprolite profile: (a) MgO (wt. %); (b) Zn; (c) molar Fe; (d) molar Mn (e) Zn isotope ratios ($\delta^{66/64}$ $Zn_{JMCLyon}$); Zn (b), Fe (c) and Mn (d) represent ratios normalised to Nb. All diagrams are plotted against depth below the soil surface. Profile sketch from Babechuk et al. (2014). The contact between the two flows (ChQA and ChQB) is illustrated. Sample ChQB9a-d at a depth of 90 cm represent a corestone transect from centre (9d) to rim (9a). The uppermost three samples in the lower flow (ChQA10-ChQA12) constitute the porous, paleo flow-top. The pink vertical line in (a) (b) (d) (e) represents the protolith composition/ratio (ChQB12). The green bar in (e) represents the analytical uncertainty (2SD) of the protolith and also the analytical uncertainty of each sample is illustrated. The yellow field in (e) represents the compositional range of the crustal average of $\delta^{66}Zn_{JMC\text{-}Lyon}$ (+0.27 ± 0.07‰, 1SD) (Little et al., 2016).

Fig.5 Bidar laterite profile: (a) Fe_2O_3 (wt. %); (b) Zn ratios normalised to Nb. (c) Zn isotope ratios ($\delta^{66/64}Zn_{JMCLyon}$); (d) TOC (%); (e) % change in ratio of dust derived elements (Nd, Th, U) relative to the protolith (Babechuk et al., 2015); The dashed purple vertical line in (a), (b), (d) represents the protolith composition/ratio (BB1). The red bar in (c) represents the analytical uncertainty (2SD) of the protolith. The yellow field in (c) represents the compositional range of the crustal average of $\delta^{66}Zn_{JMC\text{-}Lyon}$ (+0.27 ± 0.07‰, 1SD) (Little et al., 2016).

Fig.6 (a) Binary diagram of $\delta^{66/64}Zn_{JMCLyon}$ (‰) and Fe_2O_3 (wt. %) of the Bidar laterite profile. Excluding sample BB4, a very good correlation (R^2 = 0.944) between $\delta^{66/64}Zn_{JMCLyon}$ (‰) and Fe_2O_3 (wt. %) is evident, whereas under consideration of all samples a regression line is defined that indicates a moderate correlation (R^2 = 0.622). **(b)** Cross plot of $\delta^{66/64}Zn_{JMCLyon}$ (‰) and TOC (wt. %) for samples from the Bidar laterite profile. Excluding sample BB6, a strong correlation (R^2 = 0.764) is evident, whereas the complete dataset results in a much more modest correlation (R^2 = 0.421). Analytical uncertainty of $\delta^{66/64}Zn_{JMCLyon}$ (‰) = 2SD.

Fig.7 (a) Mineralogical transformations of primary mafic phases (pyroxene, volcanic glass) in the process of saprolitisation; (b) Mineralogical transformations of pyroxene and smectite in the process of lateritisation (Anand, 2005; Noack et al., 1993). The weathering resistance of the primary Fe-Ti oxides results in the retention of some amounts of Zn with respect to the

overall soil budget. All other minerals undergo mineralogical transformations that result in a loss of Zn, so that an inherently low content of Zn in the weathering residue/soil develops. Note that the "weathering vectors" in Chhindwara (a) and Bidar (b) differ, since the incipient to intermediate weathering stages in basalt are still texturally controlled, whereas the weathering progression in the stronger weathered Bidar laterite profile increases upwards the profile, likewise to " typical textbook" soil profiles.

References

Alloway B. Soil factors associated with zinc deficiency in crops and humans. Environmental Geochemistry and Health 2009; 31: 537-548.

Alloway BJ. Zinc in soils and crop nutrition: International Zinc Association Brussels, Belgium, 2008.

Anand R. Weathering history, landscape evolution and implications for exploration. Regolith landscape evolution across Australia: A compilation of regolith landscape case studies with regolith landscape evolution models. CRC LEME Monograph 2005: 2-40.

Andersen P. Geographical approaches to micronutrient deficiencies in Himalaya. 2002.

Babechuk M, Widdowson M, Murphy M, Kamber B. A combined Y/Ho, high field strength element (HFSE) and Nd isotope perspective on basalt weathering, Deccan Traps, India. Chemical Geology 2015; 396: 25-41.

Babechuk MG, Widdowson M, Kamber BS. Quantifying chemical weathering intensity and trace element release from two contrasting basalt profiles, Deccan Traps, India. Chemical Geology 2014; 363: 56-75.

Beck RA, Burbank DW, Sercombe WJ, Riley GW, Barndt JK, Berry JR, et al. Stratigraphic evidence for an early collision between northwest India and Asia. Nature 1995; 373: 55-58.

Bermin J, Vance D, Archer C, Statham PJ. The determination of the isotopic composition of Cu and Zn in seawater. Chemical Geology 2006; 226: 280-297.

Berner E, Berner R. Global environment: water, air, and geochemical cycles. 1996.

Black RE, Victora CG, Walker SP, Bhutta ZA, Christian P, De Onis M, et al. Maternal and child undernutrition and overweight in low-income and middle-income countries. The Lancet 2013; 382: 427-451.

Bonnet NJ, Beauvais A, Arnaud N, Chardon D, Jayananda M. First 40Ar/39Ar dating of intense Late Palaeogene lateritic weathering in Peninsular India. Earth and Planetary Science Letters 2014; 386: 126-137.

Borger H, Widdowson M. Indian laterites, and lateritious residues of southern Germany: A petrographic, mineralogical, and geochemical comparison. Zeitschrift fur Geomorphologie 2001; 45: 177-200.

Brantley SL, Goldhaber MB, Ragnarsdottir KV. Crossing Disciplines and Scales to Understand the Critical Zone. Elements 2007; 3: 307-314.

Brimhall GH, Dietrich WE. Constitutive mass balance relations between chemical composition, volume, density, porosity, and strain in metasomatic hydrochemical systems: Results on weathering and pedogenesis. Geochimica et Cosmochimica Acta 1987; 51: 567-587.

Cakmak I. Tansley Review No. 111 Possible roles of zinc in protecting plant cells from damage by reactive oxygen species. New Phytologist 2000; 146: 185-205.

Chairidchai P, Ritchie G. Zinc adsorption by a lateritic soil in the presence of organic ligands. Soil Science Society of America Journal 1990; 54: 1242-1248.

769 Chen H, Savage PS, Teng F-Z, Helz RT, Moynier F. Zinc isotope fractionation during
770 magmatic differentiation and the isotopic composition of the bulk Earth. Earth and
771 Planetary Science Letters 2013; 369–370: 34-42.
772 Chenet A-L, Quidelleur X, Fluteau F, Courtillot V, Bajpai S. 40 K–40 Ar dating of the Main
773 Deccan large igneous province: Further evidence of KTB age and short duration.
774 Earth and Planetary Science Letters 2007; 263: 1-15.
775 Clift P, Gaedicke C, Edwards R, Il Lee J, Hildebrand P, Amjad S, et al. The stratigraphic
776 evolution of the Indus Fan and the history of sedimentation in the Arabian Sea.
777 Marine Geophysical Researches 2002; 23: 223-245.
778 Courtillot V, Feraud G, Maluski H, Vandamme D, Moreau MG, Besse J. Deccan flood
779 basalts and the Cretaceous/Tertiary boundary. Nature 1988; 333: 843-846.
780 Cucciniello C, Demonterova EI, Sheth H, Pande K, Vijayan A. 40Ar/39Ar geochronology
781 and geochemistry of the Central Saurashtra mafic dyke swarm: insights into magmatic
782 evolution, magma transport, and dyke-flow relationships in the northwestern Deccan
783 Traps. Bulletin of Volcanology 2015; 77: 45.
784 Dolling P, Ritchie G. Estimates of soil solution ionic strength and the determination of pH in
785 West Australian soils. Soil Research 1985; 23: 309-314.
786 Fyfe WS, Kronberg BI, Leonardos OH, Olorunfemi N. Global tectonics and agriculture: A
787 geochemical perspective. Agriculture, Ecosystems & Environment 1983; 9: 383-399.
788 Gallet S, Jahn B-m, Torii M. Geochemical characterization of the Luochuan loess-paleosol
789 sequence, China, and paleoclimatic implications. Chemical Geology 1996; 133: 67-
790 88.
791 Ganerød M, Torsvik TH, van Hinsbergen DJJ, Gaina C, Corfu F, Werner S, et al.
792 Palaeoposition of the Seychelles microcontinent in relation to the Deccan Traps and
793 the Plume Generation Zone in Late Cretaceous-Early Palaeogene time. Geological
794 Society, London, Special Publications 2011; 357: 229-252.
795 Gidigasu M. Laterite soil engineering: pedogenesis and engineering principles. Vol 9:
796 Elsevier, 2012.
797 Guinoiseau D, Gélabert A, Allard T, Louvat P, Moreira-Turcq P, Benedetti MF. Zinc and
798 copper behaviour at the soil-river interface: New insights by Zn and Cu isotopes in the
799 organic-rich Rio Negro basin. Geochimica et Cosmochimica Acta 2017; 213: 178-
800 197.
801 Hewawasam T, von Blanckenburg F, Bouchez J, Dixon JL, Schuessler JA, Maekeler R. Slow
802 advance of the weathering front during deep, supply-limited saprolite formation in the
803 tropical Highlands of Sri Lanka. Geochimica et Cosmochimica Acta 2013; 118: 202-
804 230.
805 Hooper P, Widdowson M, Kelley S. Tectonic setting and timing of the final Deccan flood
806 basalt eruptions. Geology 2010; 38: 839-842.
807 Hotz C, Brown KH. Assessment of the risk of zinc deficiency in populations and options for
808 its control. 2004; 25 (Supplement 2): S91-S204.
809 Houben D, Sonnet P, Tricot G, Mattielli N, Couder E, Opfergelt S. Impact of Root-Induced
810 Mobilization of Zinc on Stable Zn Isotope Variation in the Soil–Plant System.
811 Environmental Science & Technology 2014; 48: 7866-7873.
812 Jouvin D, Louvat P, Juillot F, Marechal C, Benedetti M. Zinc isotopic fractionation : why
813 organic matters ? Environ Sci Technol 2009; 43: 5747 - 54.
814 Juillot F, Maréchal C, Ponthieu M, Cacaly S, Morin G, Benedetti M, et al. Zn isotopic
815 fractionation caused by sorption on goethite and 2-Lines ferrihydrite. Geochimica et
816 Cosmochimica Acta 2008; 72: 4886-4900.
817 Kale VS. Fluvial geomorphology of Indian rivers: an overview. Progress in Physical
818 Geography 2002; 26: 400-433.

819 Kısakürek B, Widdowson M, James RH. Behaviour of Li isotopes during continental
820 weathering: the Bidar laterite profile, India. Chemical Geology 2004; 212: 27-44.
821 Klootwijk CT, Peirce JW. India's and Australia's pole path since the late Mesozoic and the
822 India-Asia collision. Nature 1979; 282: 605-607.
823 Krauskopf KB, Bird DK. Introduction to geochemistry. Vol 721: McGraw-Hill New York,
824 1967.
825 Kurtz AC, Derry LA, Chadwick OA, Alfano MJ. Refractory element mobility in volcanic
826 soils. Geology 2000; 28: 683-686.
827 Little SH, Vance D, McManus J, Severmann S. Key role of continental margin sediments in
828 the oceanic mass balance of Zn and Zn isotopes. Geology 2016; 44(3): 207-210.
829 Little SH, Vance D, Walker-Brown C, Landing WM. The oceanic mass balance of copper
830 and zinc isotopes, investigated by analysis of their inputs, and outputs to
831 ferromanganese oxide sediments. Geochimica et Cosmochimica Acta 2014; 125: 673-
832 693.
833 Luck J-M, Othman DB, Albarède F. Zn and Cu isotopic variations in chondrites and iron
834 meteorites: Early solar nebula reservoirs and parent-body processes. Geochimica et
835 Cosmochimica Acta 2005; 69: 5351-5363.
836 McLennan SM. Relationships between the trace element composition of sedimentary rocks
837 and upper continental crust. Geochemistry, Geophysics, Geosystems 2001; 2: n/a-n/a.
838 Mitchell C, Widdowson M. A geological map of the southern Deccan Traps, India and its
839 structural implications. Journal of the Geological Society 1991; 148: 495-505.
840 Moeller K, Schoenberg R, Pedersen R, Weiss D, Dong S. Calibration of the new certified
841 reference material ERM-AE633 and ERM-AE647 for copper and IRMM-3702 for
842 zinc isotope amount ratio determinations. Geostandards Geoanalytical Res 2012;
843 36/2: 177 - 99.
844 Molnar P, Stock JM. Slowing of India's convergence with Eurasia since 20 Ma and its
845 implications for Tibetan mantle dynamics. Tectonics 2009; 28: n/a-n/a.
846 Moynier F, Vance D, Fujii T, Savage P. The Isotope Geochemistry of Zinc and Copper.
847 Reviews in Mineralogy and Geochemistry 2017; 82: 543-600.
848 Nesbitt HW, Wilson RE. Recent chemical weathering of basalts. American Journal of
849 Science 1992; 292: 740-777.
850 Nesbitt HW, Young GM. Early Proterozoic climates and plate motions inferred from major
851 element chemistry of lutites. Nature 1982; 299: 715-717.
852 Noack Y, Colin F, Nahon D, Delvigne J, Michaux L. Secondary-mineral formation during
853 natural weathering of pyroxene; review and thermodynamic approach. American
854 Journal of Science 1993; 293: 111-134.
855 Opfergelt S, Cornélis JT, Houben D, Givron C, Burton KW, Mattielli N. The influence of
856 weathering and soil organic matter on Zn isotopes in soils. Chemical Geology 2017.
857 Paton C, Hellstrom J, Paul B, Woodhead J, Hergt J. Iolite: Freeware for the visualisation and
858 processing of mass spectrometric data. Journal of Analytical Atomic Spectrometry
859 2011; 26: 2508-2518.
860 Pokrovsky OS, Viers J, Freydier R. Zinc stable isotope fractionation during its adsorption on
861 oxides and hydroxides. Journal of Colloid and Interface Science 2005; 291: 192-200.
862 Prasad AS. Discovery of human zinc deficiency: 50 years later. Journal of Trace Elements in
863 Medicine and Biology 2012; 26: 66-69.
864 Richards FD, Hoggard MJ, White NJ. Cenozoic epeirogeny of the Indian peninsula.
865 Geochemistry, Geophysics, Geosystems 2016; 17: 4920-4954.
866 Robson A, Gilkes R. Fertilizer responses (N, P, K, S, micronutrients) on lateritic soils in
867 southwestern Australia—a review. International Seminar on Laterization Processes.
868 Oxford and IBH Publishing Co. Oxford,, England, 1980, pp. 381-390.

869 Schmidt PW, Prasad V, Ramam PK. Magnetic ages of some Indian laterites.
870 Palaeogeography, Palaeoclimatology, Palaeoecology 1983; 44: 185-202.
871 Schoene B, Samperton KM, Eddy MP, Keller G, Adatte T, Bowring SA, et al. U-Pb
872 geochronology of the Deccan Traps and relation to the end-Cretaceous mass
873 extinction. Science 2015: 182-184.
874 Sossi PA, Halverson GP, Nebel O, Eggins SM. Combined Separation of Cu, Fe and Zn from
875 Rock Matrices and Improved Analytical Protocols for Stable Isotope Determination.
876 Geostandards and Geoanalytical Research 2015; 39: 129-149.
877 Spicer R, Yang J, Herman A, Kodrul T, Aleksandrova G, Maslova N, et al. Paleogene
878 monsoons across India and South China: Drivers of biotic change. Gondwana
879 Research 2017; 49: 350-363.
880 Tang Y-J, Zhang H-F, Ying J-F, Su B-X. Widespread refertilization of cratonic and circum-
881 cratonic lithospheric mantle. Earth-Science Reviews 2013; 118: 45-68.
882 Taylor SR, McLennan SM, McCulloch MT. Geochemistry of loess, continental crustal
883 composition and crustal model ages. Geochimica et Cosmochimica Acta 1983; 47:
884 1897-1905.
885 Ubide T, McKenna CA, Chew DM, Kamber BS. High-resolution LA-ICP-MS trace element
886 mapping of igneous minerals: In search of magma histories. Chemical Geology 2015;
887 409: 157-168.
888 Vance D, Matthews A, Keech A, Archer C, Hudson G, Pett-Ridge J, et al. The behaviour of
889 Cu and Zn isotopes during soil development: Controls on the dissolved load of rivers.
890 Chemical Geology 2016; 445: 36-53.
891 Vanderkluysen L, Mahoney JJ, Hooper PR, Sheth HC, Ray R. The Feeder System of the
892 Deccan Traps (India): Insights from Dike Geochemistry. Journal of Petrology 2011;
893 52: 315-343.
894 Viers J, Oliva P, Nonell A, Gélabert A, Sonke JE, Freydier R, et al. Evidence of Zn isotopic
895 fractionation in a soil–plant system of a pristine tropical watershed (Nsimi,
896 Cameroon). Chemical Geology 2007; 239: 124-137.
897 Viets FGJ, Boawn LC, Crawford CL. Zinc contents and deficiency symptoms of 26 crops
898 grown on a zinc-deficient soil. Soil Science 1954; 78: 305-316.
899 Wang P, Clemens S, Beaufort L, Braconnot P, Ganssen G, Jian Z, et al. Evolution and
900 variability of the Asian monsoon system: state of the art and outstanding issues.
901 Quaternary Science Reviews 2005; 24: 595-629.
902 Wedepohl KH, Correns CW. Handbook of geochemistry. 1969.
903 Wessells KR, Brown KH. Estimating the global prevalence of zinc deficiency: results based
904 on zinc availability in national food supplies and the prevalence of stunting. PloS one
905 2012; 7: e50568.
906 Widdowson M. Tertiary palaeosurfaces of the SW Deccan, Western India: implications for
907 passive margin uplift. Geological Society, London, Special Publications 1997; 120:
908 221-248.
909 Widdowson M. Laterite and ferricrete. Geochemical Sediments and Landscapes 2007: 45-94.
910 Widdowson M, Cox KG. Uplift and erosional history of the Deccan Traps, India: Evidence
911 from laterites and drainage patterns of the Western Ghats and Konkan Coast. Earth
912 and Planetary Science Letters 1996; 137: 57-69.
913 Widdowson M, Pringle MS, Fernandez OA. A Post K–T Boundary (Early Palaeocene) Age
914 for Deccan-type Feeder Dykes, Goa, India. Journal of Petrology 2000; 41: 1177-1194.
915 Wiederhold JG. Metal Stable Isotope Signatures as Tracers in Environmental Geochemistry.
916 Environmental Science & Technology 2015; 49: 2606-2624.

Wimpenny J, Gannoun A, Burton KW, Widdowson M, James RH, Gíslason SR. Rhenium and osmium isotope and elemental behaviour accompanying laterite formation in the Deccan region of India. Earth and Planetary Science Letters 2007; 261: 239-258.

Web reference

USGS, 1997. https://earthquake.usgs.gov/data/crust/maps.php

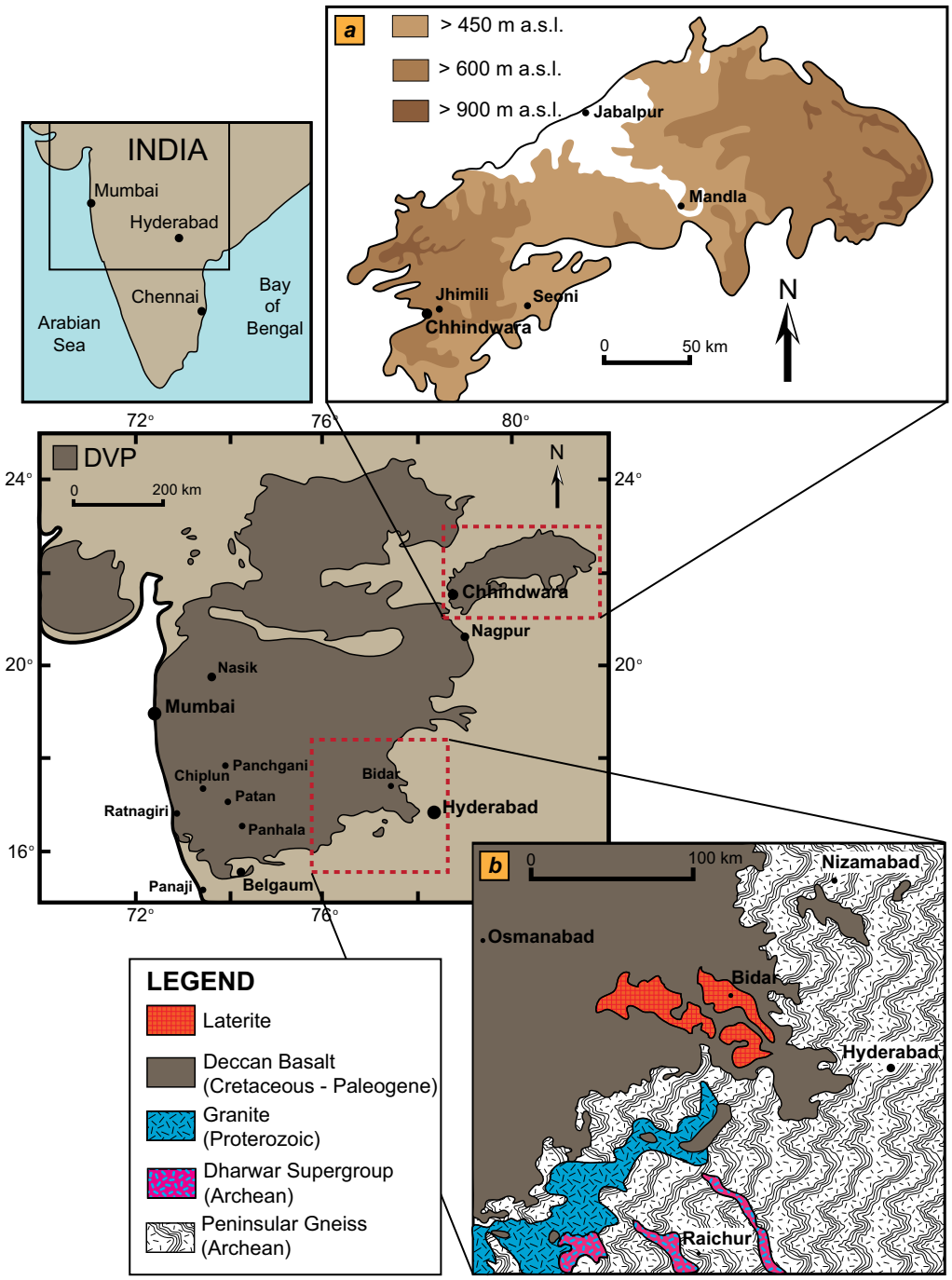

Figure 1
Suhr et al. 2018

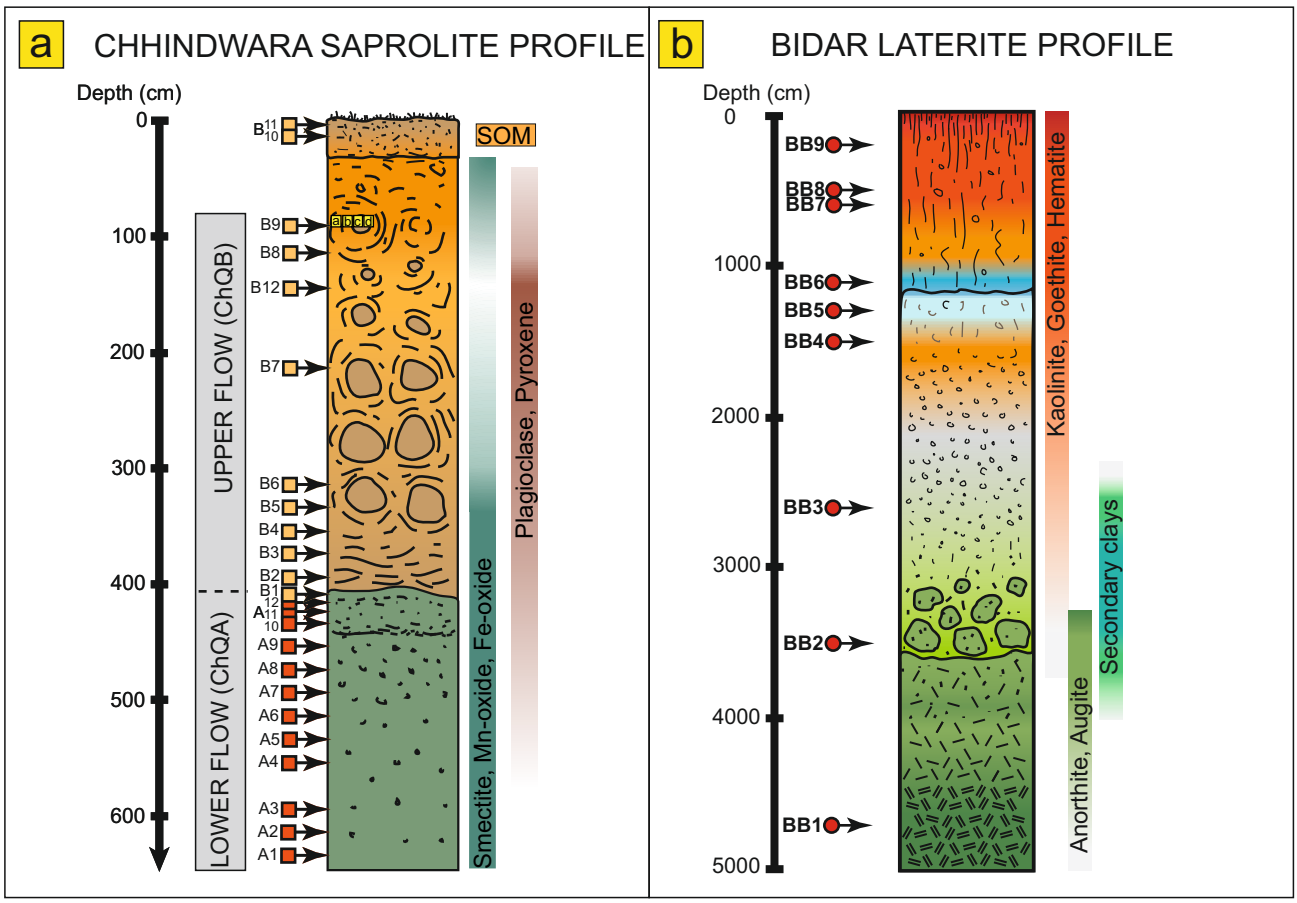

Figure 2
Suhr et al. 2018

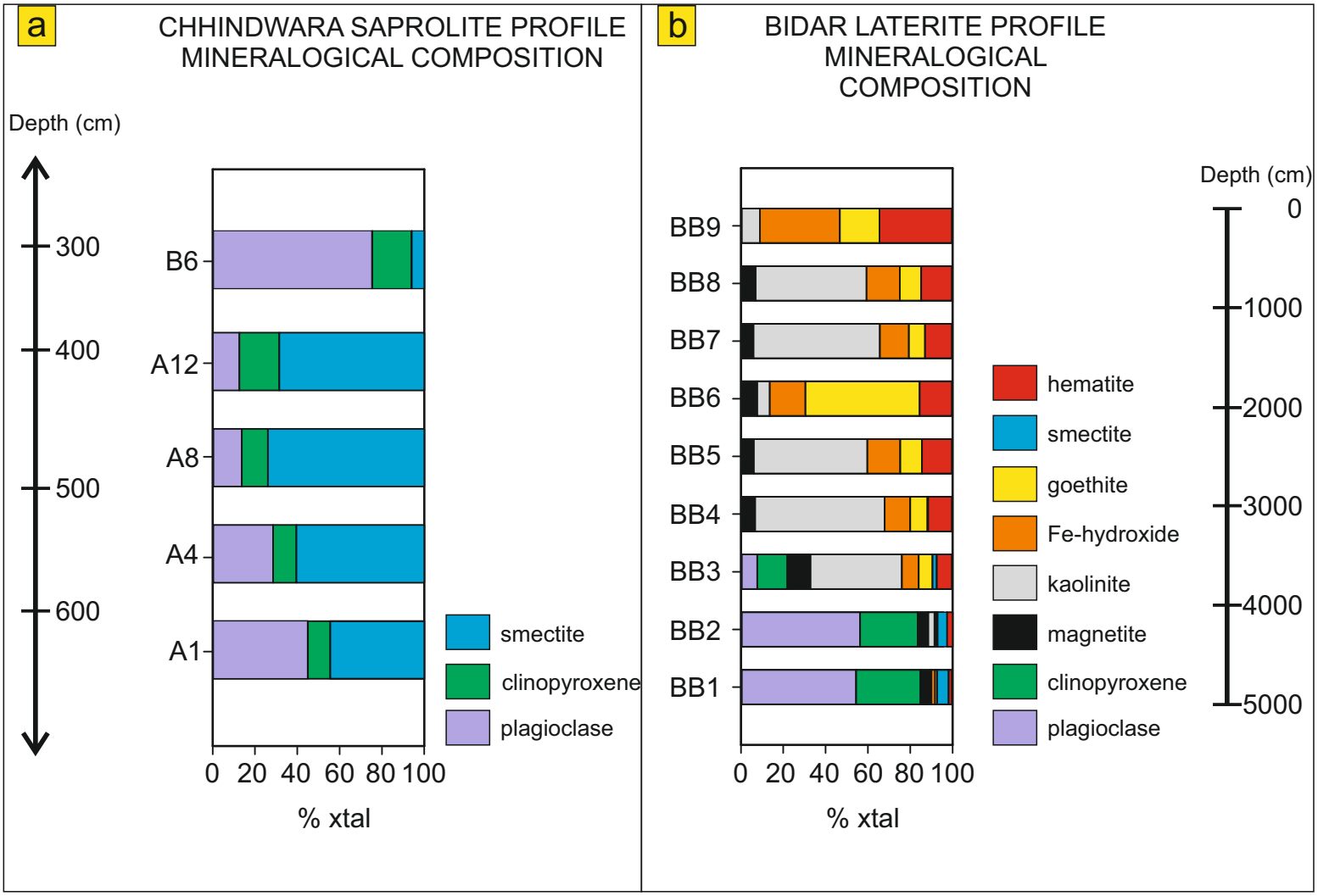

Figure 3
Suhr et al. 2018

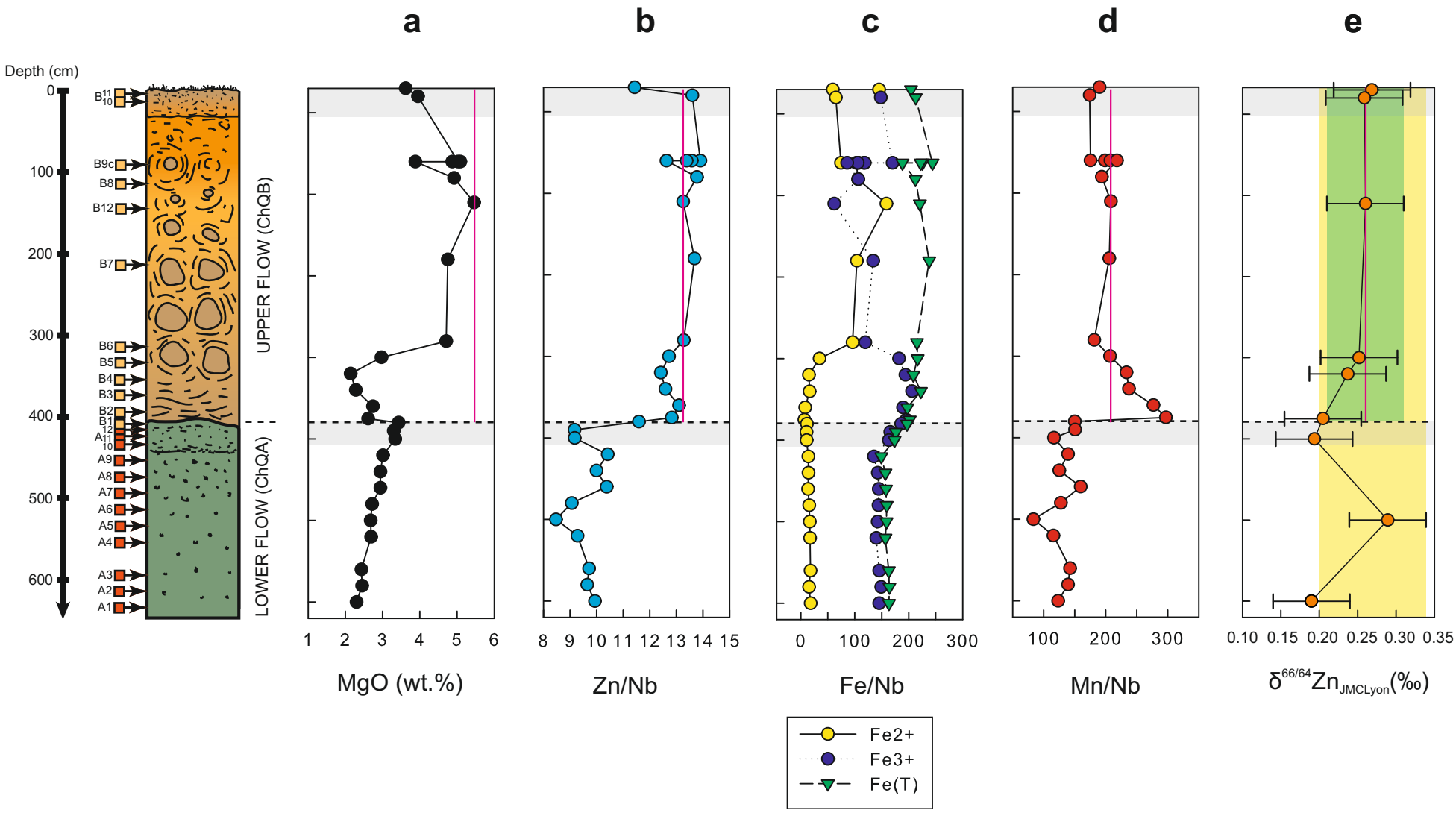

Figure 4
Suhr et al. 2018

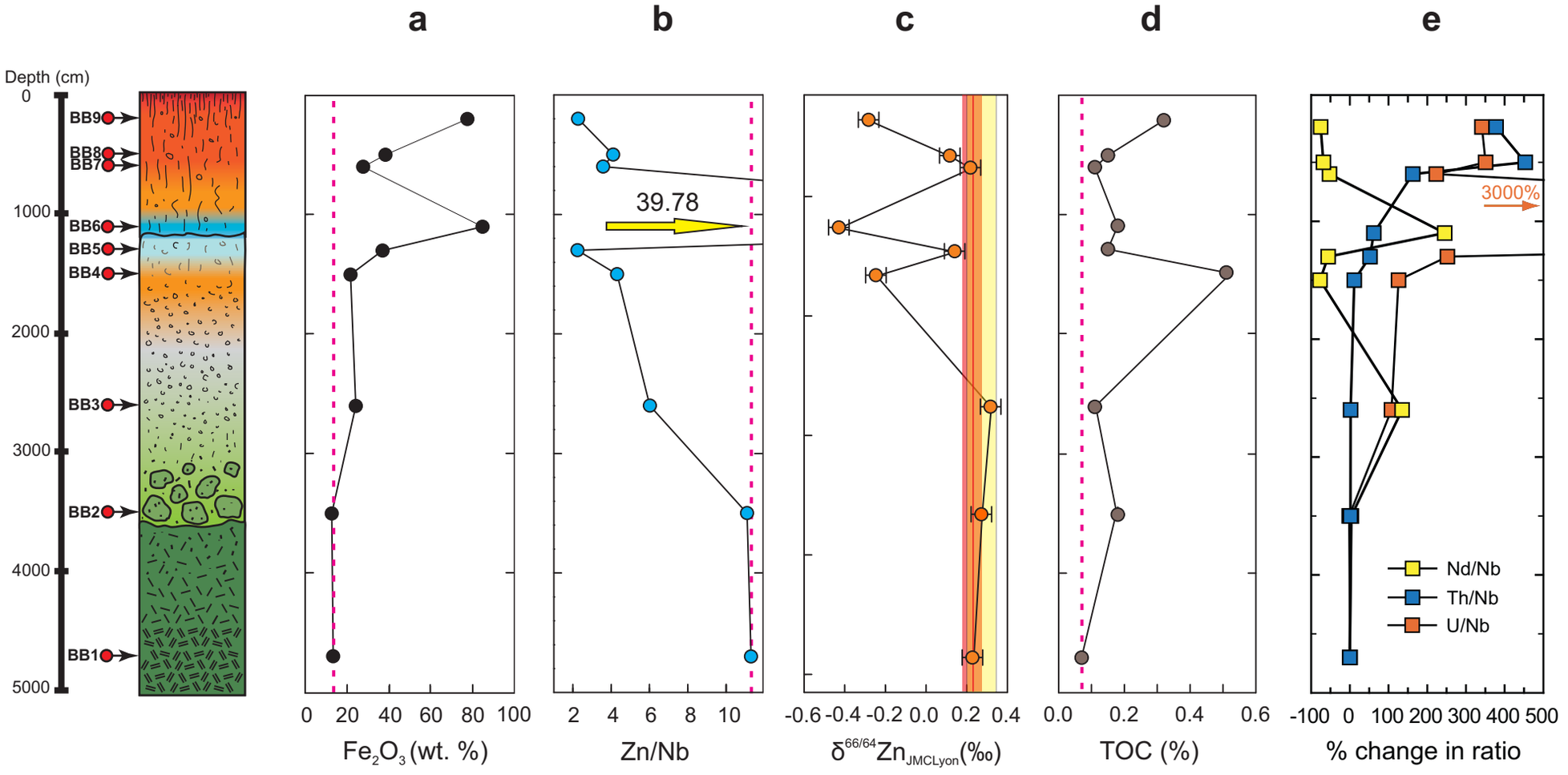

Figure 5
Suhr et al. 2018

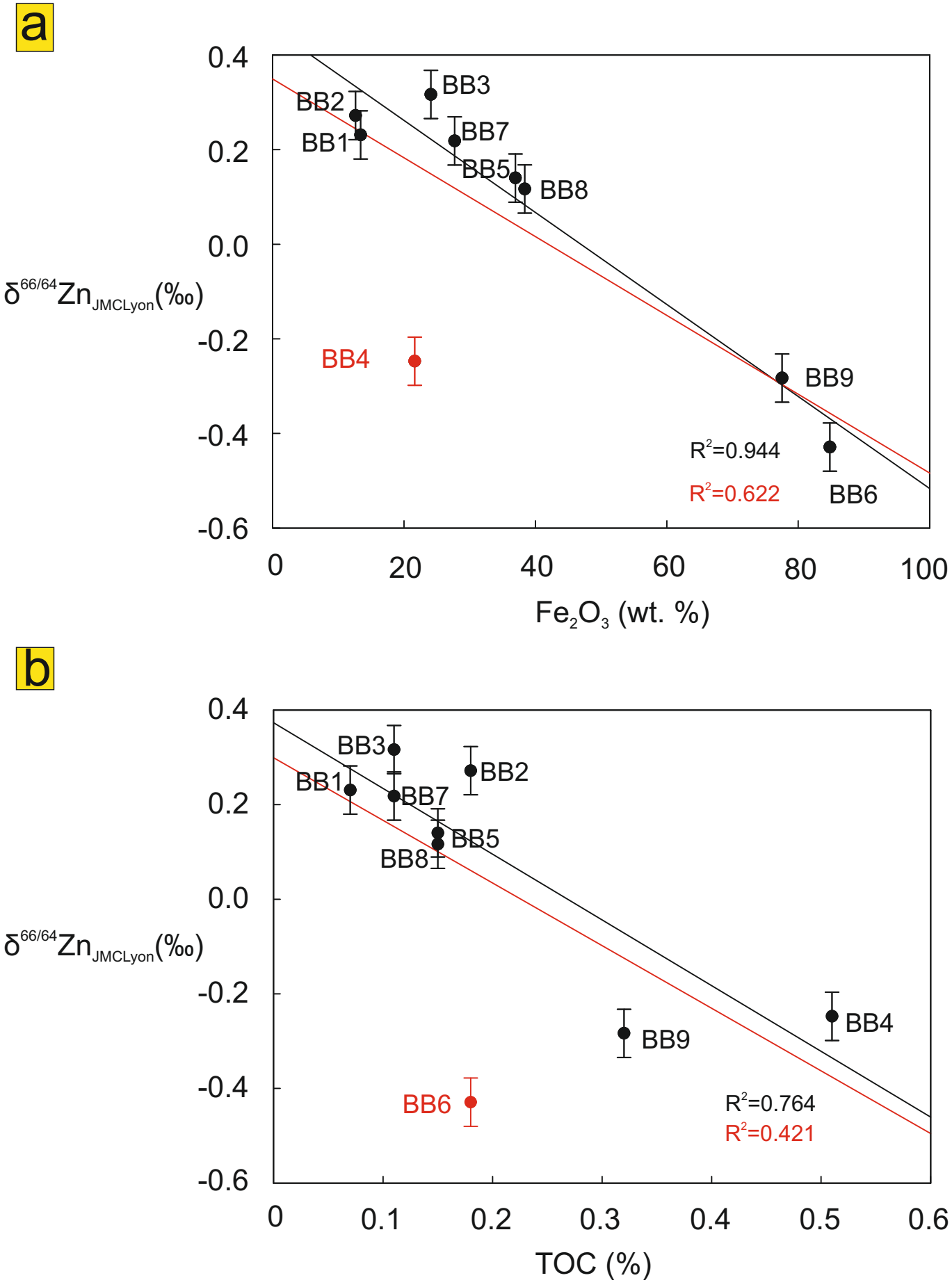

Figure 6
Suhr et al. 2018

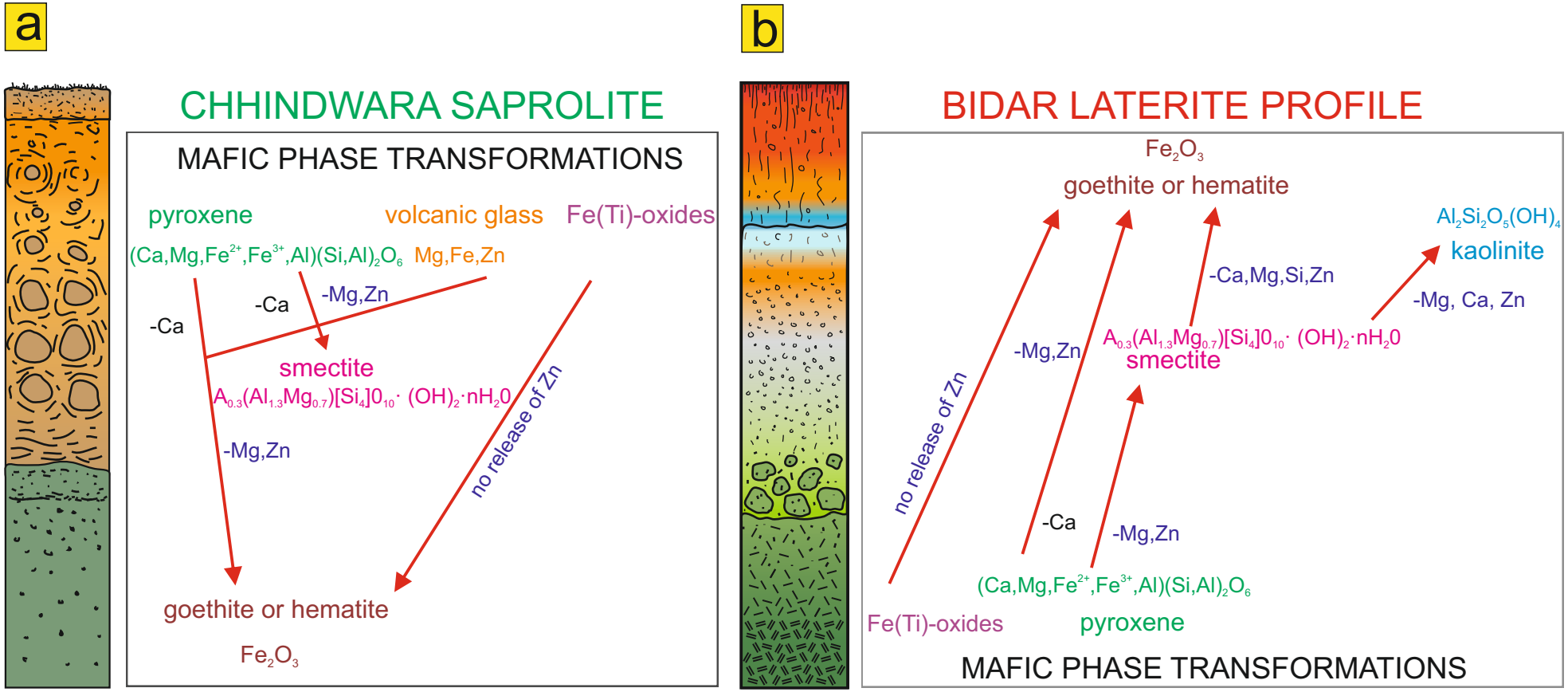

Figure 7
Suhr et al. 2018

Table 1

Table 1 Major (wt%) and trace element (µg/g) concentrations, weathering indices ($MIA_{(O)}$, CIA)[a], relative % loss (R) of Mn[b], Zn, as well as Zn isotope compositions of the Chhindwara and Bidar profiles.

Chhindwara saprolite profile

Sample	Description	Depth (cm)	MgO	Zn/Nb	Mn/Nb	$MIA_{(O)}$	CIA	Fe^{2+}/Nb	Fe^{3+}/Nb	∑Fe/Nb	$R_{Mn\%}$	Zn	$R_{Zn\%}$	$\delta^{66}Zn_{IRMM-3702}$	$\delta^{66}Zn_{JMC-Lyon}$	2SE	$\Delta^{66}Zn_{sample-protolith}$
			wt%					*molar*	*molar*	*molar*	*/Nb*	*(µg/g)*	*/Nb*				
ChQB11	Topsoil	0	3.62	11.43	190.14	57	57	59.23	144.95	204.18	− 8.69	139.63	− 13.78	− 0.022	0.268	0.020	0.008
ChQB10	Topsoil	10	3.95	13.60	174.17	56	58	64.82	148.30	213.13	− 16.36	145.15	2.62	− 0.031	0.259	0.019	− 0.001
ChQB9d	Corestone	90	5.03	13.90	175.60	67	38	74.32	169.90	244.22	− 15.67	112.09	4.89				
ChQB9c	Least weathered corestone	90	5.09	13.58	198.90	56	38	106.92	118.54	225.46	− 4.48	114.77	2.45				
ChQB9b	Corestone	90	4.87	13.38	207.73	42	39	116.87	105.58	222.45	− 0.24	116.32	0.98				
ChQB9a	Corestone	90	3.88	12.62	218.05	44	47	102.67	85.77	188.44	4.71	122.63	− 4.76				
ChQB8		110	4.92	13.77	193.73	38	39	105.97	106.53	212.50	− 6.97	126.64	3.91				
ChQB12	Parent rock	140	5.46	13.25	208.23	38	36	158.65	62.00	220.65	0	113.38	0.00	− 0.030	0.260	0.018	−
ChQB7		210	4.75	13.68	205.81	41	43	103.91	134.07	237.98	− 1.16	113.25	3.21				
ChQB6		310	4.71	13.28	181.59	39	40	95.89	119.46	215.35	− 12.8	118.91	0.17				
ChQB5		330	2.97	12.72	206.99	40	54	34.63	181.93	216.56	− 0.6	123.77	− 4.00	− 0.038	0.252	0.022	− 0.009
ChQB4		350	2.14	12.42	233.47	41	67	14.89	193.87	208.76	12.12	127.69	− 6.31	− 0.053	0.237	0.015	− 0.023
ChQB3		370	2.28	12.59	237.31	50	70	16.23	206.23	222.47	13.96	127.33	− 5.04				
ChQB2		390	2.74	13.10	277.01	56	79	7.86	189.49	197.35	33.03	139.16	− 1.17				
ChQB1		405	2.61	12.83	296.98	57	78	6.43	195.53	201.96	42.62	130.44	− 3.24	− 0.085	0.205	0.012	− 0.055
ChQA12		410	3.43	11.59	150.04	68	74	11.06	185.85	196.91	− 27.95	119.65	− 12.55				
ChQA11		420	3.3	9.17	150.66	68	73	10.46	165.74	176.20	− 27.65	103.68	− 30.83				
ChQA10		430	3.34	9.17	116.71	70	72	10.72	163.02	173.74	− 43.95	109.53	− 30.82	− 0.096	0.194	0.013	− 0.067
ChQA9		450	3.01	10.42	139.16	68	80	13.81	135.54	149.34	− 33.17	144.93	− 21.41				
ChQA8		470	2.94	10.00	125.11	70	79	14.00	142.71	156.72	− 39.92	136.12	− 24.59				
ChQA7		490	2.94	10.38	159.64	69	79	13.18	144.59	157.77	− 23.34	135.96	− 21.68				
ChQA6		510	2.72	9.06	127.63	68	78	15.33	143.89	159.21	− 38.71	121.01	− 31.61				
ChQA5		530	2.68	8.47	83.47	69	78	16.40	142.43	158.84	− 59.92	117.90	− 36.09	− 0.001	0.289	0.020	0.029
ChQA4		550	2.69	9.28	115.75	68	74	16.94	139.85	156.79	− 44.41	130.38	− 29.99				
ChQA3		590	2.43	9.72	142.52	63	74	17.83	145.19	163.02	− 31.56	137.30	− 26.68				
ChQA2		610	2.45	9.65	139.30	63	72	15.12	148.97	164.09	− 33.1	134.06	− 27.23				
ChQA1		630	2.3	9.94	123.39	64	71	18.06	145.19	163.25	− 40.74	130.95	− 25.04	− 0.100	0.190	0.024	− 0.070

Bidar laterite profile

Sample	Description	Depth (cm)	Zn/Nb	$MIA_{(O)}$	CIA	Fe_2O_3	TOC	Zn	$R_{Zn\%}$	$\delta^{66}Zn_{IRMM-3702}$	$\delta^{66}Zn_{JMC-Lyon}$	2SE	$\Delta^{66}Zn_{sample-protolith}$
						wt%	*wt%*	*(µg/g)*	*/Nb*				
BB-9	Nodular laterite	200	2.27	99.3	99.7	77.53	0.32	31.83	− 79.91	− 0.573	− 0.283	0.012	− 0.514
BB-8	Vermiform laterite	500	4.10	99.4	99.7	38.37	0.15	69.33	− 63.70	− 0.174	0.116	0.019	− 0.115
BB-7	Base of laterite	600	3.58	98.6	99.9	27.7	0.11	51.83	− 68.35	− 0.072	0.218	0.014	− 0.013
BB-6	Base of laterite/top of saprolite	1100	39.78	99.4	100	84.81	0.18	224.59	252.07	− 0.719	−0.429	0.020	− 0.660
BB-5	Saprolitised basalt (grey/blue colour)	1300	2.24	98.8	99.9	36.95	0.15	52.57	− 80.18	− 0.150	0.140	0.013	− 0.091
BB-4	Reddened saprolite	1500	4.31	91.3	90.4	21.64	0.51	80.10	− 61.88	− 0.537	− 0.247	0.012	− 0.478
BB-3	Deeply weathered basalt (saprolite)	2600	6.02	97.8	99.9	24.1	0.11	114.03	− 46.72	0.026	0.316	0.020	0.085
BB-2	Basalt with minor alterations	3500	11.09	35.5	36	12.63	0.18	113.15	− 1.83	− 0.018	0.272	0.016	0.041
BB-1	Unaltered basalt	4700	11.30	35	36.5	13.4	0.07	104.64	-	− 0.059	0.231	0.014	−

[a] Major elements, trace elements, $MIA_{(O)}$ and CIA values described in detail in Babechuk et al. (2014). [b] Mn is only presented for the Chhindwara profile

Elemental and isotopic behaviour of Zn in Deccan basalt weathering profiles: Implications for chemical weathering from bedrock to laterite and links to Zn deficiency in tropical soils

Supplementary Material

Nils Suhr, Ronny Schoenberg, David Chew, Carolina Rosca, Mike Widdowson, Balz S. Kamber

TABLE OF CONTENTS

Bulk rock X-Ray diffraction patterns

1. *Methodology and analytical description*

1.1. Enterprise Building at Trinity College (Dublin, Ireland)

The Bruker D5000 in TCD Geochemistry has a 2.2 kW Cu long fine focus (0.4 x 12mm filament), with the following optical configuration: 2.5° primary soller, 1 mm aperture diaphragm, 1 mm scattered radiation diaphragm, no secondary soller, 0.2 mm detector diaphragm and a secondary curved graphite monochromator ahead of the scintillation counter. A scan of sample was made from 3 to 40° 2θ at a speed of 1 seconds / 0.02° step at 40 kV and 40 mA. Sample rotation was applied. The bulk powder XRD patterns are reported as the relative intensity (I/Io) vs. 2Ɵ angle (Cu Kα). Bruker AXS, Diffrac.EVA software (2012 Release, Version 3.0) was used to interpret the trace and the International Centre for Diffraction Data, Pennsylvania, PDF-4 3+ database to provide phase matching. Further, standardless semiquantitative phase abundances were obtained applying the RIR (reference intensity ratios) method. Clay mineral identification were conducted using the techniques described by Hillier (2002) and Starkey et al. (1984) and were best in agreement to Hillier et al. (2002). For clay mineral analyses, a representative 1 g portion of each sample was placed in 50 ml graduated cylinder and DI water added up to the 50 ml mark. The sample was shaken thoroughly, subjected to ultrasound for 5 minutes and then allowed to stand for 3 hours. (Where flocculation occurred, 0.5 ml of 0.1M sodium hexametaphosphate was added and the dispersion process repeated). After 3 hours, a nominal <2 µm fraction was removed (from 39 mm below the surface as per Stokes' Law) using a thin diameter glass pipette and pipetted onto the surface of a Si wafer ('zero-background') and allowed to dry overnight at room temperature. The sample was run on the XRD and then placed in an ethylene glycol vapour (at 60 °C) overnight, before being rerun so a comparison between the air dried and glycol-solvated sample could be made.

1.2 Central Analytical Facility (CAF) at Laurentian University (Sudbury, Ontario, Canada)

Samples ChQB2, ChQB3 and ChQB10 were selected for qualitative X-ray diffraction (XRD) analysis. All patterns were obtained from dry, untreated powders. No attempt at detailed phyllosilicate analysis (e.g., ethylene glycol treatment or heating) was made. The XRD measurement was performed with a Phillips PW 1729 X-ray diffractometer operated at 40 kV/30

mA using Fe filtered Co Kα radiation. The powders were scanned from 5° to 75° (2Θ) with a step-size of 0.02° and a dwell time of 2 s at each step. Phase identification was performed using PANalytical's X'Pert HighScore.

2. *Results of bulk rock X-ray diffraction patterns*

2.1 Chhindwara profile

Eight samples from different sample heights and weathering degrees were selected for qualitative XRD analyses (Figs. 1, 2). Additionally, the XRD patterns of Fig. 1 were used for quantitative XRD analyses. The XRD patterns in Fig. 1 follow in the progression of their weathering intensity, starting with the least weathered sample CHQB6 at the bottom of the figure. The XRD patterns show that the primary mineral phases in both flows of the Chhindwara profile consist of plagioclase and clinopyroxene. The peak intensities, however, differ in the measured samples. Generally, the peak intensities of plagioclase and clinopyroxene decrease with higher degrees of weathering. By contrast, secondary phases of smectite (nontronite) and Fe-oxide increase in the stronger weathered samples. Amorphous phases in the samples can be inferred from the background intensities. They also increase in samples that are characterised by higher intensities of weathering. The degree of formation of secondary phases is lower in the upper volcanic flow in comparison to the lower volcanic flow. Moreover, both flows in the Chhindwara profile comprise the same mineral phases that only differ in their abundance, except for sample ChQB10 where carbon was detected as an additional phase. Unfortunately, the techniques applied to identify different phases of clay minerals (Starkey et al., 1984) were not able to deliver better data compared to the bulk XRD analysis and confirmed that the peaks of smectite match best with nontronite. Likely, high quantities of amorphous clay minerals and oxides complicate attempts in identifying the different mineral phases in relatively low weathered soil sections (i.e., in regolith), since XRD analyses are most suitable for the identification of crystalline mineral phases. In addition, the Chhindwara bedrock in the lower volcanic flow derived from a dolerite sill and consist of ca 20% volcanic glass (see chapter 3), which further complicates attempts in identifying the mineral phases. Hence, the quantification of smectite, plagioclase and clinopyroxene represents an estimate of the mineral phase abundance in the different sections of the Chhindwara profile.

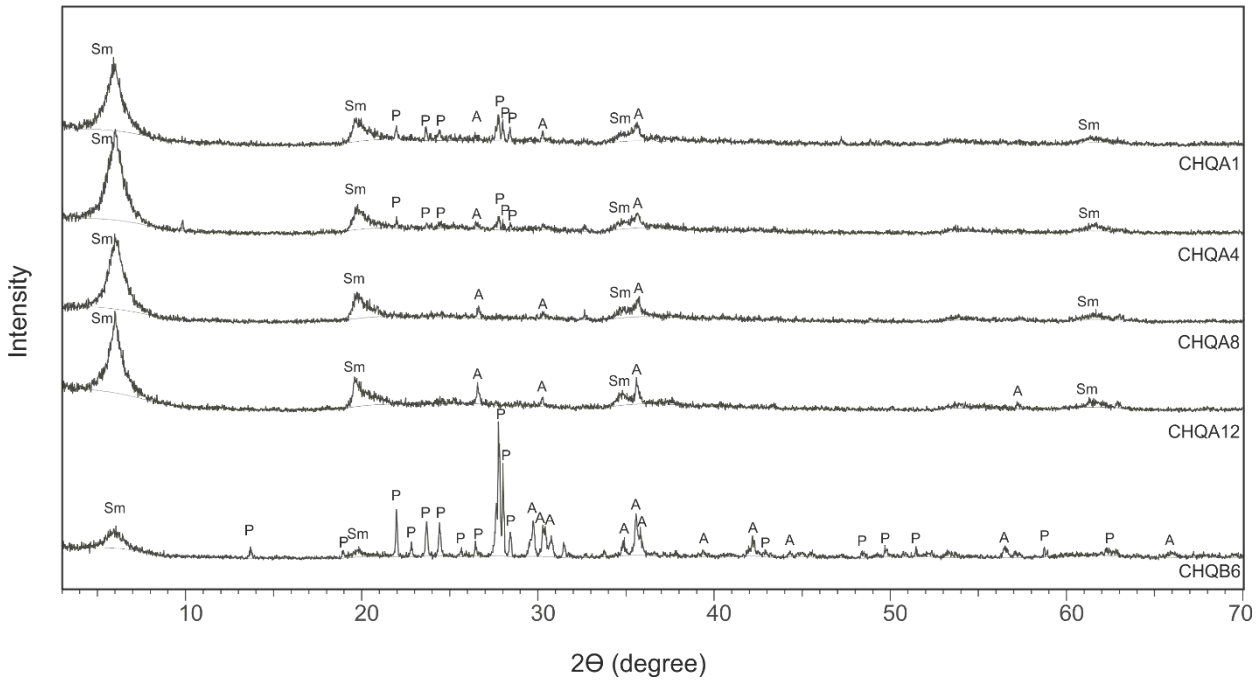

Fig. S1. Bulk powder XRD patterns of representative samples (CHQB6, CHQA12, CHQA8, CHQA4 and CHQA1) of the Chhindwara saprolite profile. P, plagioclase; A, augite; Sm, smectite.

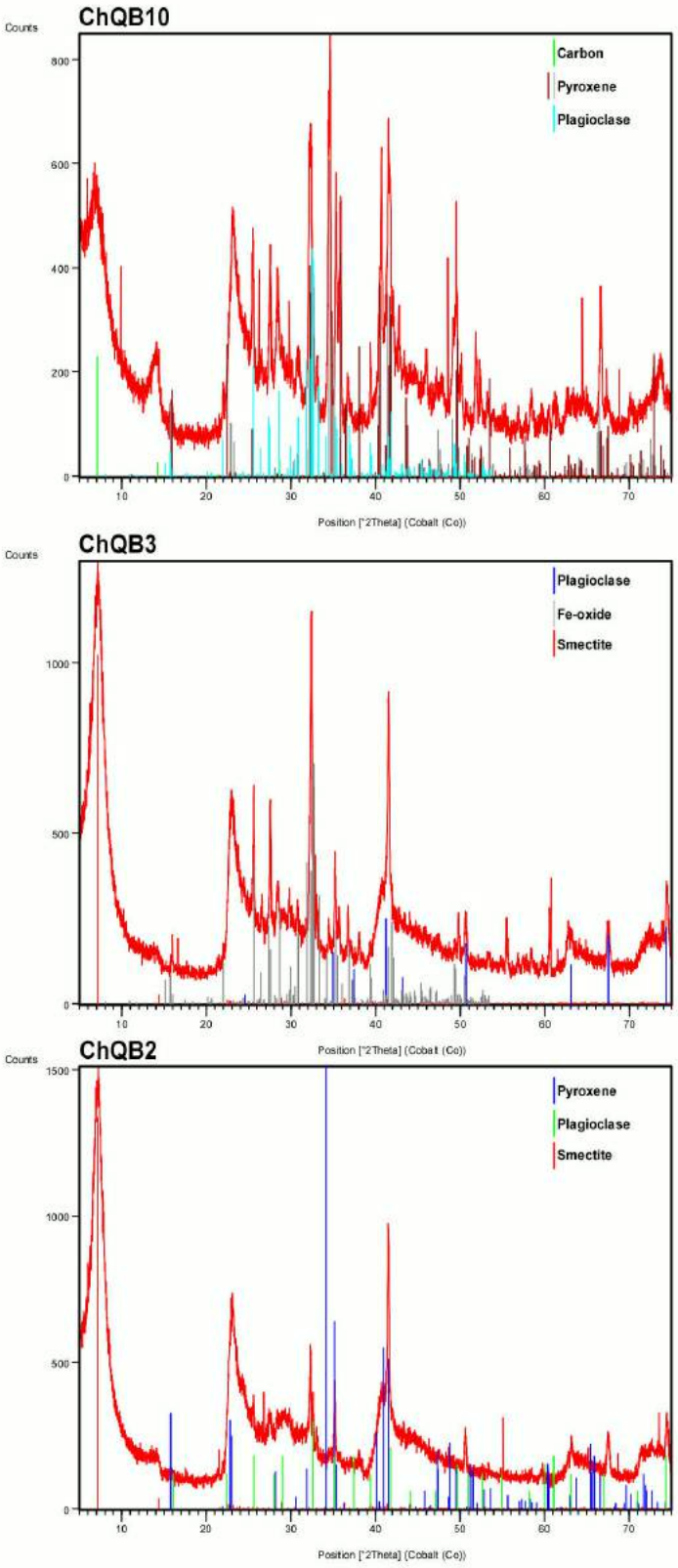

Fig. S2. Representative XRD diagrams of samples ChQB10, ChQB3, and ChQB2.

2.2 Bidar laterite profile

All nine samples of the Bidar profile were selected for qualitative X-ray diffraction (XRD) analysis. The patterns were collected on dry, untreated powders. No attempt at detailed phyllosilicate analysis (e.g., ethylene glycol treatment or heating) was made. The XRD patterns of all 9 samples are illustrated in Fig. 3 and in order of increasing sample height. For smectite, the best phase matches were nontronite and montmorillonite and detected in samples BB1-BB2. Further, plagioclase, clinopyroxene (augite) and magnetite were identified as primary mineral phases. In samples BB3-BB5, the primary phases have been almost completely replaced by secondary mineral phases and the formation of kaolinite, goethite, iron-hydroxide and hematite is evident. An exception is represented by sample BB6 (palaeo-watertable), where goethite dominates. In addition, hematite, iron-hydroxide, and minor amounts of magnetite and kaolinite were identified. Above the palaeo-watertable, kaolinite is significantly enriched, but the peak intensity of kaolinite decreases with the intensity of chemical depletion towards the nodular cap (BB9), whereas the peak intensities of hematite, goethite, and iron-hydroxide increase.

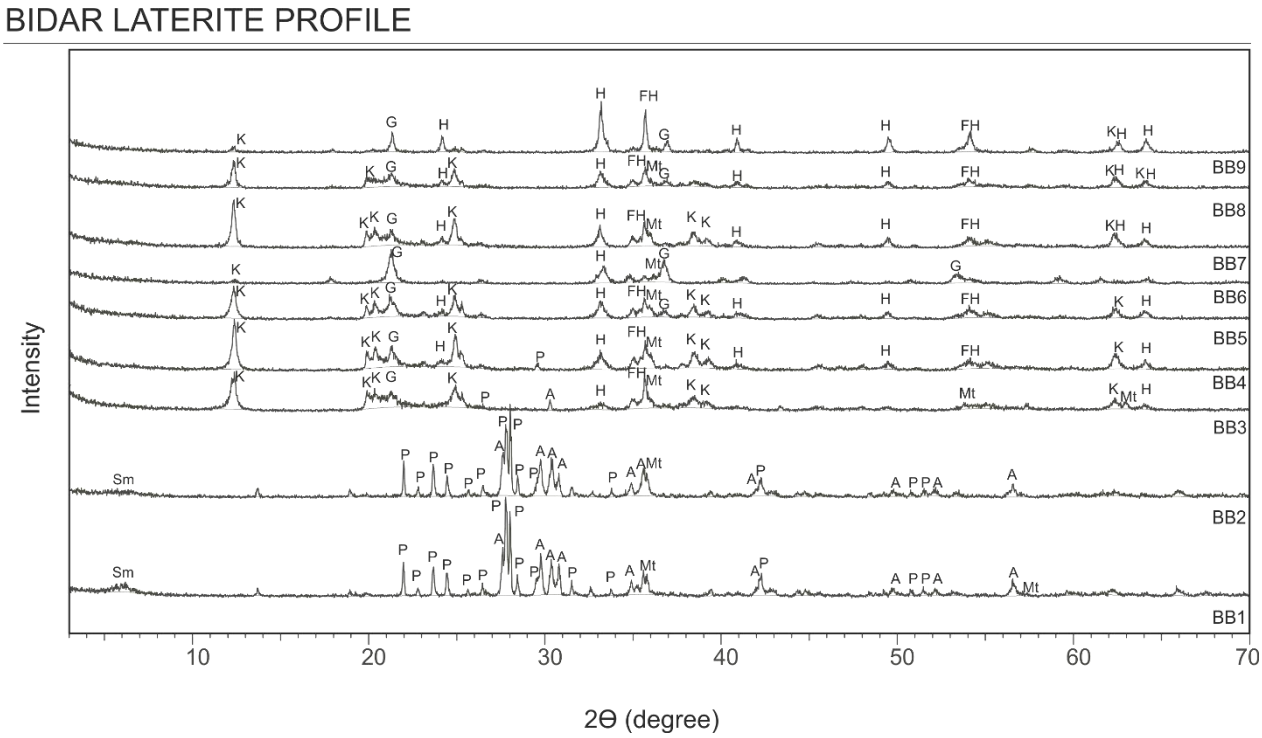

Fig. S3. Bulk powder XRD patterns of all samples of the Bidar laterite profile. P, plagioclase; A, augite; Mt, magnetite; Sm, smectite; K, kaolinite; G, goethite; FH, iron-hydroxide (hematite); H, hematite.

Petrography

3. Microscopy of the Chhindwara and Bidar bedrock

The following two subsections include thin section descriptions of the Chhindwara and Bidar bedrock that were recently sampled (January 2016). Thin section photomicrographs include plane polarised light (PPL) and cross polarised light (XPL) images. Overall, the modal abundance of the identified minerals in thin section correlates with the quantitative XRD analyses of the Bidar bedrock. In addition, the modal abundance of clinopyroxene and smectite of the Chhindwara bedrock are similar to the calculated values from the RIR method, except for plagioclase. Our petrographic observations therefore confirm the reliability of the applied RIR method, notably for the Bidar laterite profile.

3.1 Chhindwara bedrock

This thin section consists of plagioclase (ca. 45%), clinopyroxene (25%; augite), 5% orthopyroxene (hypersthene) and primary Fe-Ti oxide (5 %). The grain sizes are relatively homogenous, and plagioclase and clinopyroxene crystals typically have sizes of 400-600 μm. In places, they even reach sizes of up to 1000 μm. Furthermore, volcanic glass (20%) has sizes of up to 400-600 μm in the thin section and occurs also as small inclusions within pyroxene, plagioclase and the matrix. The large aggregates of volcanic glass are already altered and have developed clay coatings. In addition, a minor amount of isotropic material around a few clinopyroxene rims indicates the presence of altered glass. Particularly in the centre of the volcanic glass, clay particles are oriented perpendicular to the pore walls, which confirms their authigenic origin (Kühn et al., 2010). Moreover, the occurrence of primary minerals within the altered glass aggregates supports an authigenic origin. Weathering products also formed along cracks in clinopyroxene. Moreover, subgrain formation and atypical interference colours provide evidence of minor alteration in clinopyroxene. In total, these weathering products comprise 5% of the thin section. Secondary weathering products consist also of hematite, goethite, and oxy-hydroxides, but occur only as accessory phases in the rock.

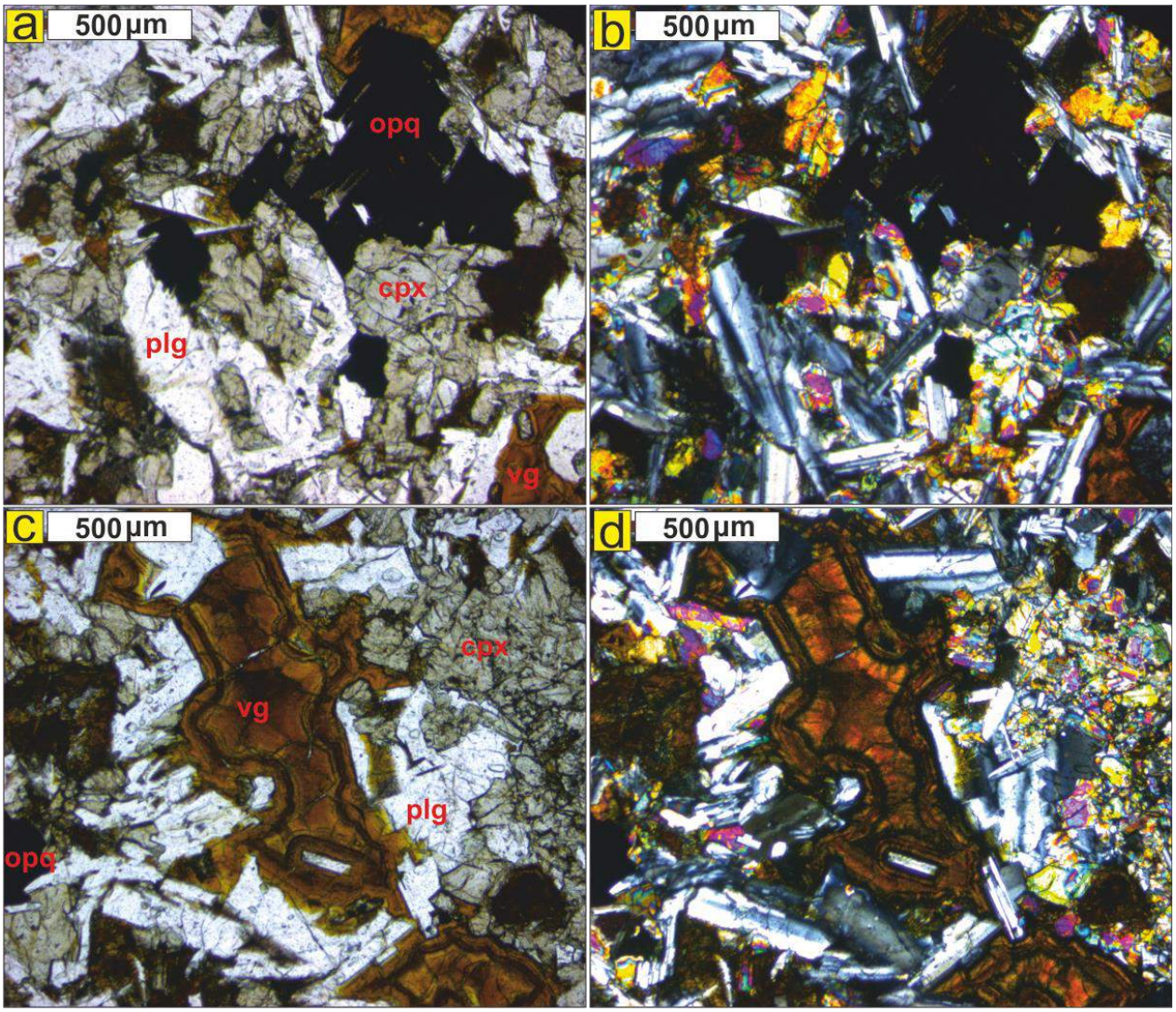

144

145 **Fig. S4.** Photomicrographs of the Chhindwara saprolite bedrock under ppl (a, c) and xpl (b, d). All major phases in
146 the profile are illustrated in the images. Plg = plagioclase; cpx = clinopyroxene; vg= volcanic glass; opq = Fe-Ti
147 oxide.

148

149 3.2 Bidar bedrock

150 The bedrock is composed of a fine grained matrix that consists of euhedral-subhedral shaped,
151 twinned plagioclase laths (ca. 55 %), augite and minor amounts of hypersthene (30%), primary
152 Fe-Ti oxide (5 %) and glass (ca. 5-10 %). In places, phenocrysts of augite and plagioclase occur.
153 In a few places within the matrix, minor amounts of plagioclase and augite have been replaced by

clay minerals. In particular, volcanic glass has been altered to clays and secondary Fe-Mn oxides. Furthermore, a few minerals have been completely altered.

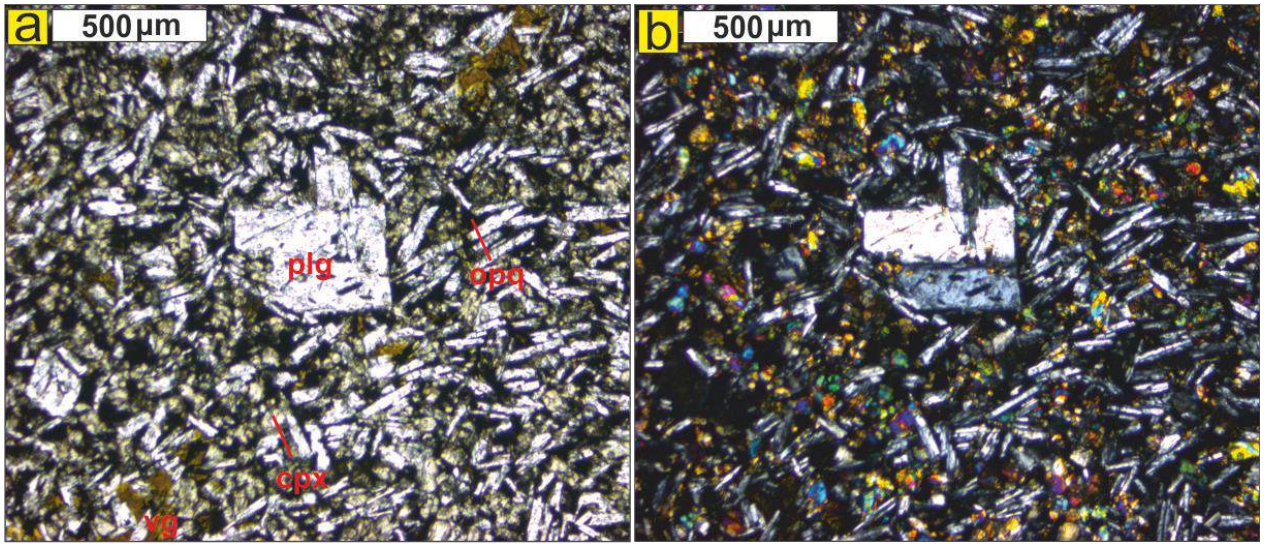

Fig. S5. Photomicrographs of the Bidar laterite bedrock under ppl (a) and xpl (b). In the centre, a phenocryst of plagioclase is surrounded by a fine grained matrix of pyroxene, plagioclase, primary Fe-Ti oxide and volcanic glass. Plg = plagioclase; cpx = clinopyroxene; vg= volcanic glass; opq = Fe-Ti oxide.

LA-ICP-MS element maps of Zn, Mg and Fe distribution

4. Figures

4.1 Chhindwara bedrock

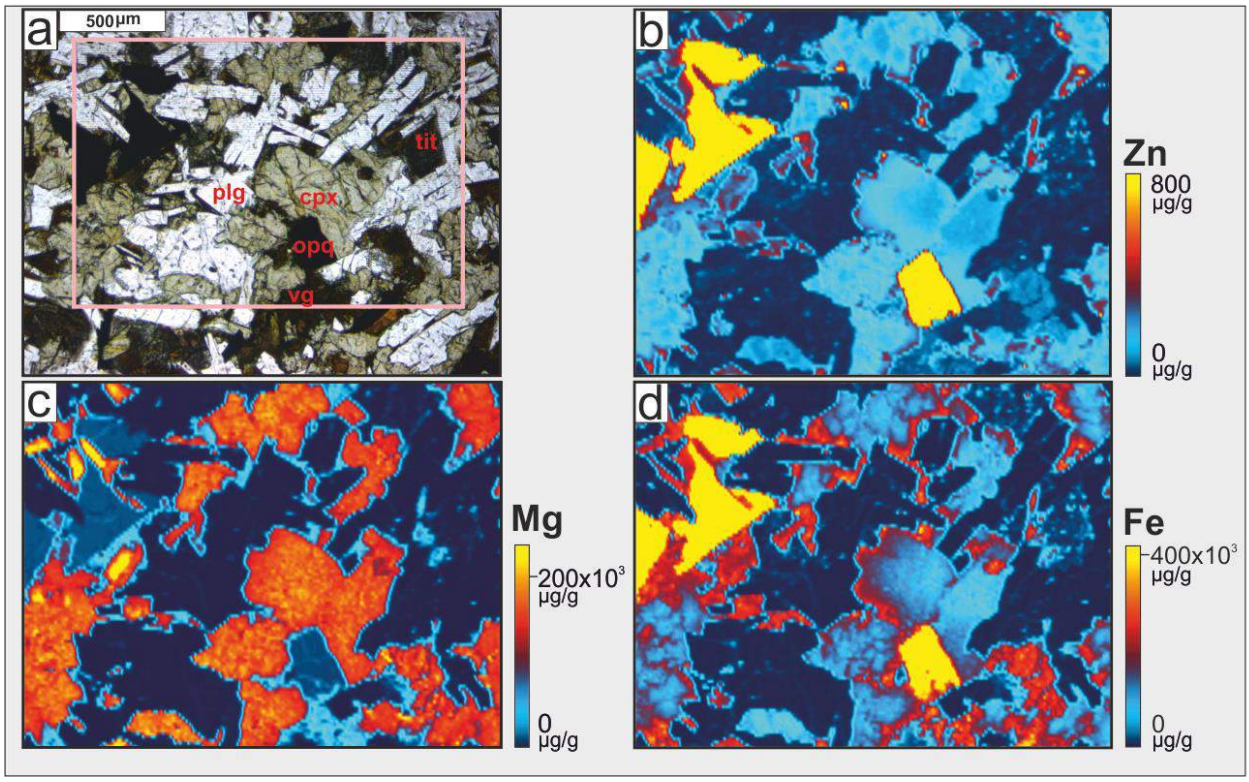

Fig. S6. (a) Photomicrograph under ppl of Fe-Mg rich clinopyroxene (cpx), volcanic glass (vg), plagioclase (plg), primary Fe-Ti oxide (opq = opaque) and titanite (tit). Volcanic glass occurs as inclusions in all silicate minerals and the matrix. The pink frame delineates the area that was laser ablated. (b) Semi-quantitative LA-ICP-MS compositional maps of Zn, (c) Mg and (d) Fe. It is obvious that weathering resistant primary Fe-Ti oxide is most Zn enriched and that clinopyroxene and volcanic glass host moderate amounts of Zn. In addition, titanite contains minor amounts of Zn but occurs only as accessory phase in the Chhindwara bedrock. Zn from the primary Fe-Ti oxide is unlikely to be released during weathering. Chemical breakdown of the Fe-Mg silicates appears to happen with the concomitant breakdown of volcanic glass, so that Mg and Zn are simultaneously released from the weathering front, whereas oxidised Fe remains in the profile.

192 4.2 Altered silicate minerals and volcanic glass of Chhindwara bedrock

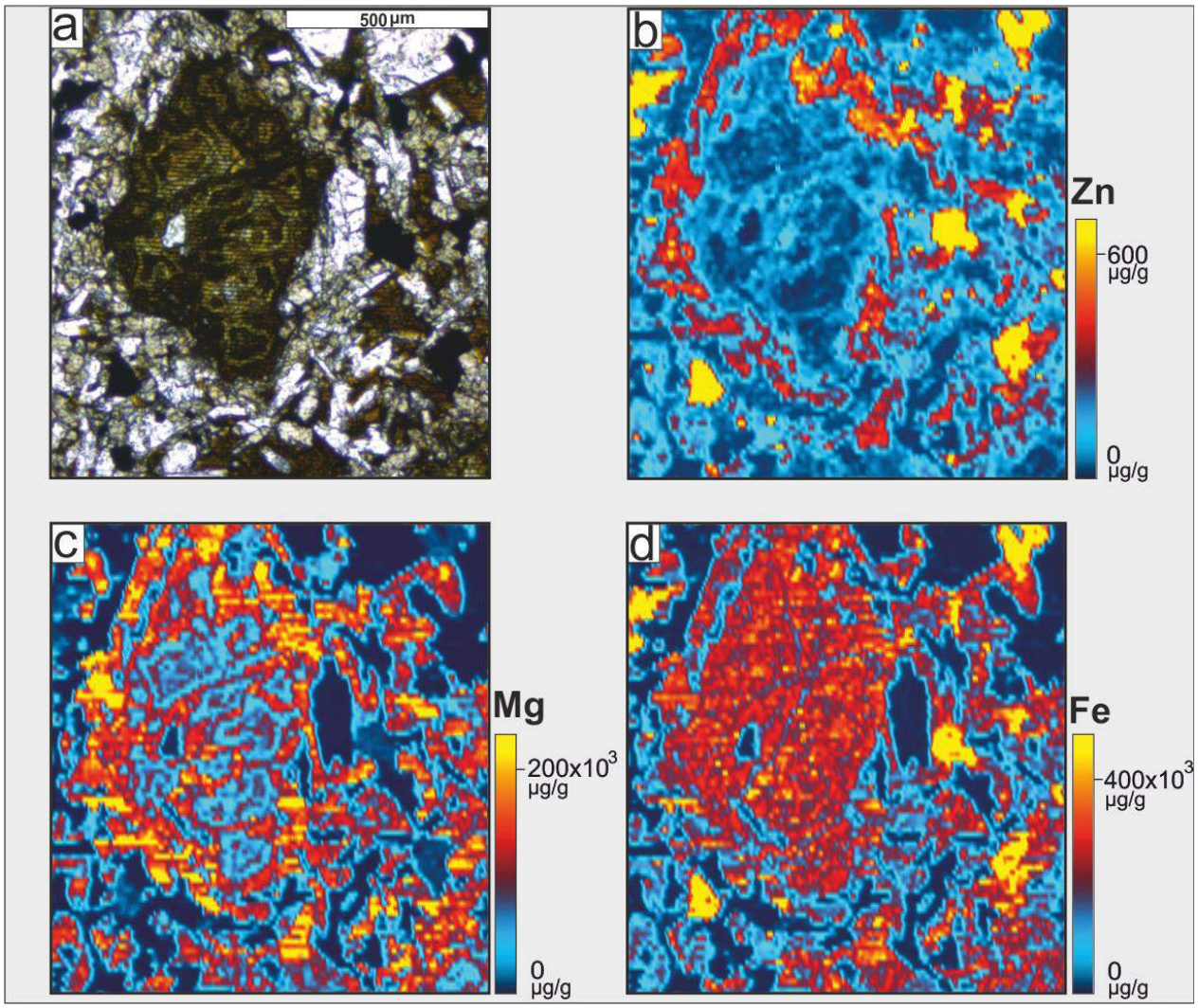

193

194 **Fig. S7.** (a) Photomicrograph under ppl of altered Mg-Fe silicate and volcanic glass from the bedrock of the lower
195 volcanic flow of the Chhindwara profile. Semi-quantitative LA-ICP-MS compositional maps of Zn (b), Mg (c), and
196 Fe (d). The trace element maps indicate that Zn substituted for Mg and Fe. Mg and Zn were already released in parts,
197 whereas oxidative weathering resulted in the immobilisation of Fe.

198

199

200

201

202

203

4.3 Bidar bedrock, palaeowater-table, nodular cap

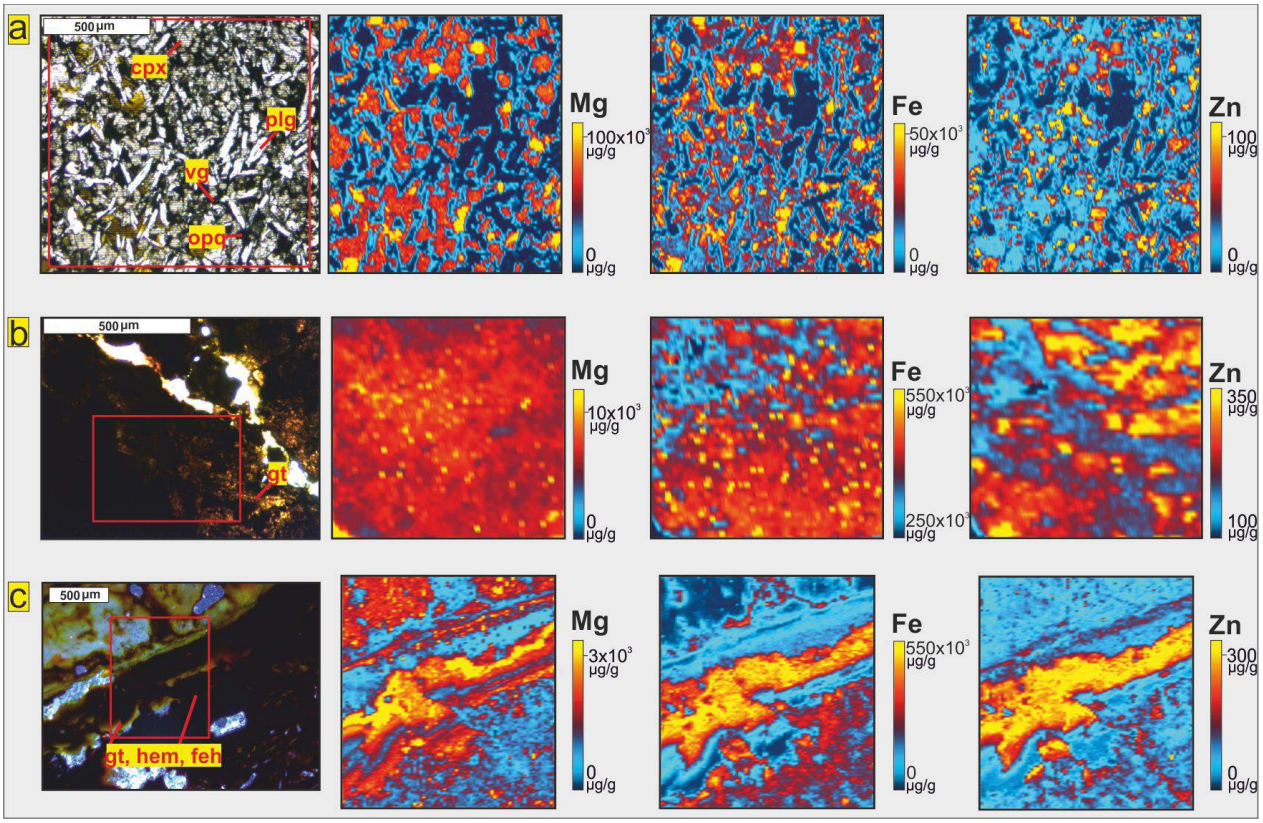

Fig. S8. Photomicrograph under ppl of the (a) bedrock (clinopyroxene (cpx), volcanic glass (vg), plagioclase (plg), primary Fe-Ti oxide (opq = opaque)) (b) palaeo-watertable, (gt = goethite) and (c) nodular cap of the Bidar laterite profile (hem = hematite; feh = iron-hydroxide) with semi-quantitative LA-ICP-MS compositional maps of Mg, Fe, and Zn. The red frame in each photomicrograph delineates the area that has been laser ablated. (a) The trace element maps indicate that Zn substituted for Mg and Fe. Clinopyroxene and primary Fe-Ti oxides host Zn (b) In the photomicrograph, mainly goethite is visible and enriched in Fe and Zn and both concentrations derived from an extraneous source. (c) In the centre, a vein composed of iron hydroxide, goethite and hematite is visible that is enriched in Fe and Zn. Particularly, below the vein lower but still high concentrations of Fe are visible, whereas only in places moderately to high concentrations of Zn are evident. This indicates that Zn in the primary iron oxides remained immobile and is inherent, whereas in newly formed iron oxides very low concentrations of Zn occur.

References

Hillier, S., 2002. Quantitative analysis of clay and other minerals in sandstones by X-ray powder diffraction (XRPD). In: Worden, R. and Sadoon, M. (eds) Clay Mineral Cements in Sandstones (Special Publication 34 of the IAS). ISBN: 978-1-4051-0587-3, 520 pages. Wiley-Blackwell.

Kühn P, Aguilar J, Miedema R. Textural pedofeatures and related horizons. Interpretation of micromorphological features of soils and regoliths. Elsevier, Oxford 2010: 217-250.

Starkey HC, Blackmon PD, Hauff PL. The routine mineralogical analysis of clay-bearing samples. Bulletin, 1984.

Supplementary table

Results of replicate BCR-2 and BHVO-2 analyses

	BHVO-2	*2σ*	*BCR-2*	*2σ*
1	0.351	0.028	0.297	0.028
2	0.298	0.040	0.278	0.040
3	0.297	0.041	0.265	0.041
average	*0.315*	*0.036*	*0.280*	*0.036*